Astronomy & Astrophysics manuscript no. aa36299-19
February 8, 2022
©ESO 2022

arXiv:2001.06400v1 [astro-ph.SR] 17 Jan 2020

The ALMA-PILS survey: Inventory of complex organic molecules towards IRAS 16293–2422 A

S. Manigand[1], J. K. Jørgensen[1], H. Calcutt[2], H. S. P. Müller[3], N. F. W. Ligterink[4], A. Coutens[5], M. N. Drozdovskaya[4], E. F. van Dishoeck[6, 7], and S. F. Wampfler[4]

[1] Niels Bohr Institute & Centre for Star and Planet Formation, University of Copenhagen, Øster Voldgade 5–7, DK-1350 Copenhagen K., Denmark
[2] Department of Space, Earth and Environment, Chalmers University of Technology, 41296, Gothenburg, Sweden
[3] I. Physikalisches Institut, Universität zu Köln, Zülpicher Str. 77, 50937 Köln, Germany
[4] Center for Space and Habitability (CSH), University of Bern, Gesellschaftsstrasse 6, 3012 Bern, Switzerland
[5] Laboratoire d'Astrophysique de Bordeaux, Univ. Bordeaux, CNRS, B18N, allée Geoffroy Saint-Hilaire, 33615 Pessac, France
[6] Leiden Observatory, Leiden University, PO Box 9513, NL-2300 RA Leiden, The Netherlands
[7] Max-Planck Institut für Extraterrestrische Physik (MPE), Giessenbachstr. 1, 85748 Garching, Germany

Received ??? / Accepted ???

ABSTRACT

Context. Complex organic molecules are detected in many sources in the warm inner regions of envelopes surrounding deeply embedded protostars. Exactly how these species form remains an open question.
Aims. This study aims to constrain the formation of complex organic molecules through comparisons of their abundances towards the Class 0 protostellar binary IRAS 16293–2422.
Methods. We utilised observations from the Atacama Large Millimetre/submillimetre Array (ALMA) Protostellar Interferometric Line Survey (PILS) of IRAS 16293–2422. The species identification and the rotational temperature and column density estimation were derived by fitting the extracted spectra towards IRAS 16293–2422 A and IRAS 16293–2422 B with synthetic spectra. The majority of the work in this paper pertains to the analysis of IRAS 16293–2422 A for a comparison with the results from the other binary component, which have already been published.
Results. We detect 15 different complex species, as well as 16 isotopologues towards the most luminous companion protostar IRAS 16293–2422 A. Tentative detections of an additional 11 isotopologues are reported. We also searched for and report on the first detections of methoxymethanol (CH_3OCH_2OH) and *trans*-ethyl methyl ether (t-$C_2H_5OCH_3$) towards IRAS 16293–2422 B and the follow-up detection of deuterated isotopologues of acetaldehyde (CH_2DCHO and CH_3CDO). Twenty-four lines of doubly-deuterated methanol (CHD_2OH) are also identified.
Conclusions. The comparison between the two protostars of the binary system shows significant differences in abundance for some of the species, which are partially correlated to their spatial distribution. The spatial distribution is consistent with the sublimation temperature of the species; those with higher expected sublimation temperatures are located in the most compact region of the hot corino towards IRAS 16293–2422 A. This spatial differentiation is not resolved in IRAS 16293–2422 B and will require observations at a higher angular resolution. In parallel, the list of identified CHD_2OH lines shows the need of accurate spectroscopic data including their line strength.

Key words. astrochemistry – stars: formation – stars: protostars – ISM: molecules – ISM: individual objects: IRAS 16293–2422

1. Introduction

Complex organic molecules (COMs, i.e. molecules containing six or more atoms with at least one carbon atom; Herbst & van Dishoeck 2009) are observed in various interstellar environments, ranging from very cold, dense collapsing cloud cores (e.g. Bacmann et al. 2012; Taquet et al. 2017) to protoplanetary discs (e.g. Öberg et al. 2015; Walsh et al. 2016; Favre et al. 2018), as well as in low- and high-mass star-forming regions (e.g. Blake et al. 1987; Fayolle et al. 2015; Bergner et al. 2017; Ceccarelli et al. 2017; Ospina-Zamudio et al. 2018; Bøgelund et al. 2019). Meteorite measurements (Ehrenfreund et al. 2001; Botta & Bada 2002), comet coma observations (Bockelée-Morvan et al. 2000; Crovisier et al. 2004; Biver et al. 2014), and in situ *Rosetta* mission measurements (Le Roy et al. 2015; Altwegg et al. 2017) have revealed complex organic molecules, such as glycolaldehyde (CH_2OHCHO), ethylene glycol ($(CH_2OH)_2$), and glycine. The presence of complex and even pre-biotic species suggests that some of these molecules that formed during the earliest stage of stellar formation are preserved until the formation of small bodies. The extent to which the most complex species were formed at the earliest evolutionary stage of the protosolar nebula and how they were preserved or transformed during the formation of planetesimals remain open and complex questions.

In this study, we focus on the formation of COMs during the deeply embedded Class 0 stage. Class 0 protostars are characterised by an envelope that is rich in diverse molecules, where most of the mass of the system is gathered (Andre & Montmerle 1994). COMs may be observed in the inner regions of the envelope, which is close to their host protostar, where the temperature exceeds the water ice desorption temperature of ∼100 K. These molecule-rich regions are called hot cores for high-mass protostars and hot corinos for low-mass counterparts. At submillimetre wavelengths, most of the lines originate from com-

plex species. The measured COM abundances are typically between 10^{-7} and 10^{-11} with respect to H_2 (e.g. Herbst & van Dishoeck 2009). In general, the formation of COMs is thought to occur on ice surfaces through a succession of different processes that are initiated by efficient hydrogenation of simple ice species, for example, CO, which leads to the efficient production of methanol (CH_3OH; Garrod & Herbst 2006; Garrod et al. 2008; Fuchs et al. 2009; Chuang et al. 2018). During the collapse of the pre-stellar core, the temperature starts to increase during the so-called warm-up phase, and more complex species form and desorb into the gas phase in the hot corino. The resulting abundances of these species in the gas depend on the initial abundances of the precursors in the parent cloud, but they are also very sensitive to the physical conditions of the pre-stellar and protostellar phases and may thus vary significantly for different protostellar sources (Garrod 2013; Drozdovskaya et al. 2016). While the gas-phase formation pathways were not efficient enough to explain such high abundances of the COMs observed in the dense warm envelope, the recent progress in quantum chemical modelling brought attention back to the gas-phase chemistry (e.g. Balucani et al. 2015; Skouteris et al. 2018, 2019). Similar progress has been made recently in the study of the deuteration of COMs through gas-phase reactions (Skouteris et al. 2017). Careful comparisons between observations and predictions from grain surface and gas-phase reaction experiments and calculations are needed to address the relative importance for the species that are present in their different protostellar environments.

Close protostellar multiple sources, that is, systems with multiple components separated by $\lesssim$ 1000 au, are particularly interesting laboratories for studying the effect of the physical conditions with time. Indeed, the chemical evolution of such sources is expected to stem from the same initial compositions and physical conditions (gas and dust temperatures as well as ultra-violet irradiation), which are inherited from the common parental cloud. The Class 0 low-mass protostellar binary IRAS 16293–2422 (IRAS 16293 hereafter), which is located in the ρ Ophiuchus cloud complex at a distance of ∼140 pc (Dzib et al. 2018), is one of the best sources to investigate for that purpose. The components of the protostellar binary are known to be rich in COMs with abundances that are comparable to those seen towards high-mass protostars (van Dishoeck et al. 1995; Cazaux et al. 2003; Caux et al. 2011). Previous interferometric observations revealed abundance differences of specific molecules between the two protostars (Bisschop et al. 2008; Jørgensen et al. 2011, 2012); however, the origin of the differentiation is still debated. The ALMA Protostellar Interferometric Line Survey[1] (PILS, Jørgensen et al. 2016) performed an unbiased spectral survey of the system in Band 7, demonstrating the strength of ALMA for detecting new complex species towards the most compact component IRAS 16293B of the system, including CH_3Cl (Fayolle et al. 2017), CH_3NC (Calcutt et al. 2018a), HONO (Coutens et al. 2019), NH_2CN (Coutens et al. 2018), and CH_3NCO (Ligterink et al. 2017). In addition, many deuterated and less abundant isotopologues have been found for the first time in the interstellar medium (ISM) towards this source, including NHDCHO, NH_2CDO (Coutens et al. 2016), NHDCN (Coutens et al. 2018), CHD_2CN (Calcutt et al. 2018b), deuterated and ^{13}C isotopologues of CH_2OHCHO, deuterated ethanol (C_2H_5OH), ketene (CH_2CO), acetaldehyde (CH_3CHO) and formic acid (HCOOH) (Jørgensen et al. 2016, 2018), $OC^{33}S$ (Drozdovskaya et al. 2018), and doubly deuterated methyl formate (CHD_2OCHO; Manigand et al. 2018). This paper aims to study the O-bearing COMs in the other protostar IRAS 16293A of the binary system and to compare their abundances with IRAS 16293B. Because of the proximity of the two sources (5"; ∼720 au), the two sources are expected to have the same molecular heritage as their parent cloud. Therefore, any abundance difference between the sources could reveal the chemistry that occurred during the earliest evolutionary phases of this low-mass protostellar binary.

Similar comparative studies have been carried out towards the Class 0 binary protostar NGC 1333 IRAS 4A. López-Sepulcre et al. (2017) observed this source at high angular resolution with ALMA and measured the abundances of eight COMs towards the two components of the binary. The authors notice a large difference in abundance for all the species and suggest that the lack of COMs towards one of the source could be due to a lower mass, with a lower accretion rate, compared to the molecule rich counterpart. This scenario could alternatively suggest that the COM-poor source is not yet in the collapse phase resulting in the formation of the hot corino, which is consistent with the lack of evidence for the presence of a hot corino in this component (Persson et al. 2012). In contrast, both components in IRAS 16293 are known to harbour hot corinos.

In this study, we present an analysis of the PILS data taken towards IRAS 16293A, which focus on the content of the O-bearing molecules in the hot corino region. This work aims to compare the abundances found for both components of the binary system to better understand the structure and/or the chemistry of this particular binary source. This paper is organised as follows. In Section 2, we describe the observations and spectroscopic data used in this study. In Section 3, we present the results of the observations and analyse the spectrum. In Section 4, we compare the abundances with those in IRAS 16293B and discuss the different aspects of the two sources. Finally, we summarise the key points of the analysis and the discussion in Section 5.

2. Data analysis

In this section, we present the results of the oxygen-bearing COMs identification using the local thermodynamic equilibrium (LTE) analysis. In Section 2.1 we present the observations used in this study and the species identification is described in Section 2.2. The LTE model and the χ^2-fitting are detailed in Section 2.3 and 2.4, respectively. Finally, the treatment of the uncertainties and the continuum correction are addressed in Section 2.5.

2.1. Observations

We used ALMA data from the PILS survey of the low-mass protostellar binary IRAS 16293 (Jørgensen et al. 2016). The data are a combination of the 12 m dishes and the Atacama Compact Array (ACA). The observations cover the frequency range of 329.1 to 362.9 GHz with a spectral resolution of 0.244 MHz, corresponding to ∼0.2 km s^{-1}, and a restoring beam of 0.″5. The survey reaches a sensitivity of 4–5 mJy beam^{-1} km s^{-1} across the entire frequency range. The ALMA software suite CASA (McMullin et al. 2007) was used to reduce the data, except for the continuum subtraction, which was performed after the data reduction (for more details, see Jørgensen et al. 2016). The flux calibration across the spectral range is consistent with the 5% level. The spectroscopic data of all the species that are analysed in this paper are detailed in Appendix C as well as the vibra-

[1] The reduced dataset and all the publications are available on the website http://youngstars.nbi.dk/PILS/

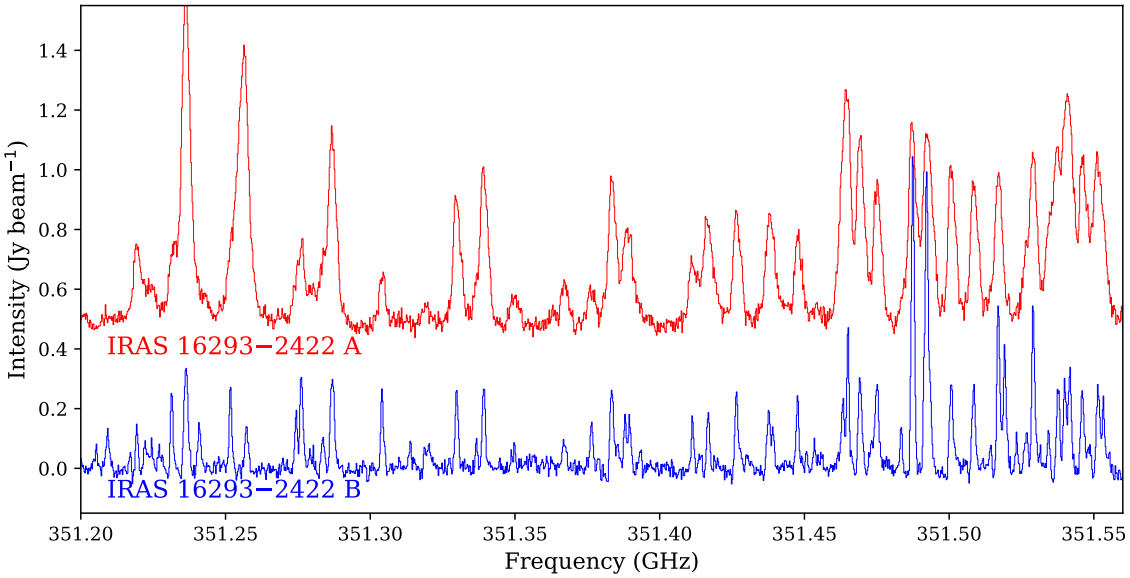


Fig. 1: Portion of the spectrum towards IRAS 16293A and IRAS 16293B in red and blue, respectively, extracted on their corresponding offset positions. IRAS 16293A spectrum is offset by 0.5 Jy beam^{-1} for illustrative purposes.

tional correction factors used, in the case of rotational temperatures that are higher than 100 K.

2.2. Species identification

In this study, oxygen-bearing COMs have been investigated towards IRAS 16293A and IRAS 16293B through the analysis of the spectral emission at one position towards each source. The continuum peak positions, the strong continuum emission, the dynamics of the gas, and the spectral line density make it difficult to analyse the molecular emission. Therefore, the spectra were extracted towards offset positions at 0″.6 from the continuum peak position in the north-east direction and 0″.5 in the south-west direction for IRAS 16293A and B, respectively. This is in agreement with the choice of the extracted spectrum position in the previous PILS studies (e.g. Calcutt et al. 2018b; Jørgensen et al. 2018; Lykke et al. 2017). Figure 1 shows the spectra towards IRAS 16293A and B. Most of the lines identified towards IRAS 16293B also appear in IRAS 16293A, albeit at different intensities, which indicates that IRAS 16293A is as rich in molecules as its companion. The line widths are typically two to three times larger towards IRAS 16293A than towards IRAS 16293B, thereby increasing the confusion due to blending effects.

The complexity of the molecular emission towards IRAS16293A and B makes the line assignment to the species difficult when based on the peak frequency alone. In some cases, a species that was not considered to be present in the source might have a significant number of transitions with frequencies coinciding with bright transitions of other species. In order to deal with such line confusion, we coupled the identification of possible O-bearing COMs present in the gas to the LTE analysis. All the species detected in the counterpart protostar IRAS16293B and their fainter isotopologues were considered as potential candidate species that compose the envelope of IRAS16293A. Additionally, related and more complex O-bearing COMs have also been added to the list of candidates, such as trans-ethyl methyl ether (t-$C_2H_5OCH_3$) and methoxymethanol (CH_3OCH_2OH).

2.3. LTE model and detection criteria

We compared the extracted spectrum with a synthetic model in order to identify and derive the abundances of species that are present in the gas. The model applies the radiative transfer equations to a homogeneous column of gas along the line of sight under the LTE assumption. Only the optically thin lines, which have a line opacity lower than 0.1, are considered in the comparison of the modelled spectrum. For each species, a single excitation temperature was assumed to describe the level populations, which we refer to as rotational temperature.

The brightness temperature $T_b(v)$ depends on the line opacity $\tau(v)$, through the relation:

$$T_b(v) = T_0 \left(\Omega \frac{1}{e^{T_0/T_{rot}} - 1} - \frac{1}{e^{T_0/T_{CMB}} - 1} \right) \left(1 - e^{-\tau(v)} \right), \quad (1)$$

with $T_0 = h\nu/k_B$, T_{rot}, the rotational temperature of the gas and the cosmic microwave background temperature $T_{CMB} = 2.73$ K. The filling factors of the gas emission, Ω, is equal to 0.5 (Jørgensen et al. 2016), corresponding to a source size of 0″.5. The source size is the same as what was used in the previous studies of IRAS 16293B based on the same dataset.

Under the LTE assumption and assuming a Gaussian profile, the line opacity is expressed as:

$$\tau(v) = \tau_0 \exp \frac{-(v - v_{LSR})^2}{2} \left(\frac{2\sqrt{2\ln 2}}{\Delta v_{FWHM}} \right)^2 \quad (2)$$

$$\text{and } \tau_0 = \frac{2\sqrt{2\ln 2}}{\Delta v_{FWHM}\sqrt{2\pi}} \frac{N_{tot} g_u A_{ul} c^3}{8\pi Q(T_{rot}) \nu_0^3} \left(e^{T_0/T_{rot}} - 1 \right) e^{-\frac{E_u}{k_B T_{rot}}} \quad (3)$$

where g_u is the upper state degeneracy, E_u is the upper state energy, A_{ul} is the Einstein coefficient of the transition, $N_mathrmtot$ is the column density, and $Q(T_{rot})$ is the partition function evaluated at T_{rot}. We note that the brightness temperature and the line opacity are functions of the velocity v, representing the velocity shift with respect to the peak velocity, v_{LSR}, which was set at the rest frequency of the modelled line. The parameters T_{ex}, N_{tot}, v_{LSR} and Δv_{FWHM}, the full line width at half-maximum in velocity units, are free parameters in the model.

The detection criteria for a species in the PILS data is mostly affected by the high density of the line present in the spectrum, which is more problematic towards IRAS16293A due to the broader lines. A line is considered to be unblended, and thus usable for the fit, in the following cases: if there is no line from another species in the $\nu_0 \pm 2$FWHM frequency range (i.e. Rayleigh criteria); and if there is a line in the $\nu_0 \pm 2$FWHM frequency range but the peak intensity of this line is lower than 10% the peak intensity of the line of interest or less than 1σ.
The frequency range considered in the Rayleigh criteria is extended to ±4FWHM at the proximity of a very optically thick blending line, for example, the low-E_{up} CH_3OH lines.

2.4. χ^2-fitting

Towards the analysed position, 0.″6 north-east of IRAS 16293A, a line width FWHM of 2.2–2.4 km s^{-1}, and a peak velocity v_{lsr} of 0.8 km s^{-1} reproduce the emission line shapes of all the species in this study, suggesting that they are indeed located in the same region around the protostar. The line width and the peak velocity towards the offset position from IRAS 16293B, which are 1.0 and 2.7 km s^{-1}, respectively, are consistent with the range of values from the previous PILS studies (0.8–1.0 km s^{-1} and 2.5–2.7 km s^{-1}, respectively, Coutens et al. 2016; Lykke et al. 2017; Calcutt et al. 2018a; Persson et al. 2018; Ligterink et al. 2017).

The species that are considered have been fitted on a grid in column density and rotational temperature, ranging from 10^{14} to 10^{18} cm^{-2} in logarithmic scale and from 75 to 300 K by increments of 5 K, respectively. Each of them were iteratively fitted from the most to least abundant and put in a reference spectrum that was taken into account for the fit of the next species.

The comparison between the observed spectrum and the model is quantified by the χ^2 minimisation, which is defined as

$$\chi^2 = \sum_{\text{lines}} \int_{\text{line profile}} \omega(v) \left(\frac{I_b(v) - T_b(v)}{\sigma_b(v)} \right)^2 \mathrm{d}v, \quad (4)$$

where $I_b(v)$ and $\sigma_b(v)$ are the line intensity and the intensity uncertainty of the extracted spectrum, respectively. We note that the intensity uncertainty includes the contribution from the calibration uncertainty σ_{cal}, the root mean square (RMS) σ_{RMS}, and the following: $\sigma_b(v) = \sqrt{\sigma^2_{RMS}(v) + \sigma^2_{cal}(v)}$.

The weighting factor $\omega(v)$ is equal to three if $T_b(v) > I_b(v)$, and it is one otherwise. In the case of this study, this weighting factor provides a better constraint on possible blending effects, which could bias the minimisation. In other words, the weighting factor increases the χ^2 value when the model is above the spectrum. We chose to break the symmetry of the model that way to allow the fitting procedure to converge to lower column density values compared to those derived with a symmetric χ^2, which could include possible contributions from species that are close enough for blending. The choice of the weighting factor value of three is arbitrary and depends on the degree of line confusion in the data.

2.5. Uncertainties and continuum corrections

The uncertainties are usually given by the covariance matrix, which is estimated in the standard χ^2 minimisation methods. However, the modified χ^2 used in this study no longer allows for the use of the covariance matrix to get the uncertainties. Instead, the uncertainties have been estimated using a simple Monte Carlo simulation, where the spectrum as well as an additional Gaussian noise of $\sigma_b(v)$ amplitude were fitted to the synthetic spectrum several times. This gives a distribution of each parameter; here, the excitation temperature and the column density are called the posterior probability distributions. This versatile method has also been successfully used to estimate the uncertainties on the 3 μm OH band model parameters as well as in reflectance spectroscopy of meteorites and asteroids (Potin et al. 2019, subm.). In summary, the posterior probability distribution of the parameters represents the distribution of the possible values that can take each parameter, given the uncertainties of the data. The formalism of this Monte Carlo simulation is detailed in Appendix B.

This statistical estimation of the uncertainties gives much lower relative errors on the excitation temperature and column density compared to the actual data relative uncertainties. This suggests that the proper statistical estimate of the errors is not conservative considering the underlying hypotheses of the LTE model and how they are handled in the minimisation. Indeed, the χ^2 minimisation assumes that the model is perfect and determines the best set of parameters to fit the observations. However, the observations include many effects that are neglected by the LTE analysis but which appear in the spectrum. These effects can be, for example, non-uniform source coverage, beam dilution, self-absorption effects, or abundance gradients of the species in the line of sight (with the associated velocity shift). Therefore, we chose to take conservative values of ∼20 and ∼30% for the rotational temperatures and the column densities relative uncertainties, respectively, for IRAS 16293A. For consistency, the relative uncertainty values used in the study of Jørgensen et al. (2018) are assumed for IRAS 16293B, that is, ∼20 and ∼10% for the rotational temperatures and the column densities, respectively.

The dust emission is treated as a continuum brightness temperature, which is directly derived from the continuum emission in the same frequency range. The high density of both sources makes it so the dust emission is partially coupled to the gas emission. In order to take into account the continuum contribution to the line emission, the correction factor A_{corr} was applied to the column density

$$A_{corr} = \frac{\Omega \frac{1}{e^{T_0/T_{rot}} - 1} - \frac{1}{e^{T_0/T_{CMB}} - 1}}{\Omega \frac{1}{e^{T_0/T_{rot}} - 1} - \Omega_{dust} \frac{1}{e^{T_0/T_d} - 1}} \quad (5)$$

in which T_d is the dust brightness temperature and Ω_{dust} is the dust emission filling factor, which is assumed to be equal to Ω. Under the LTE assumption, the use of a correction factor is equivalent to replacing T_{CMB} with the dust brightness temperature T_d in Equation 1. The dust brightness temperatures used in this paper are 30.1 K and 21.2 K towards the offset position from continuum peak positions towards IRAS16293A and B, respectively. The value of the continuum correction factor ranges from ∼1.1 at 300 K to ∼1.4 at 90 K and it does not strongly depend on the frequency across the spectral range of the PILS data.

Table 1: Best-fit results of all the detected and tentatively detected species towards IRAS 16293A.

Species	#$_{lines}$	E_{up} range (K)	T_{rot} (K)	N_{tot} (cm^{-2})	N_{tot}/N_{CH_3OH}	N_{tot}/N_{main}	isotopic ratio[a]
CH_3OH	18	61 – 1201	130 ± 26	$1.3 \pm 0.4 \times 10^{19}$			
$CH_3^{18}OH$	7	35 – 338	130 ± 26[c]	$2.3 \pm 0.6 \times 10^{16}$		$1.8 \pm 0.8 \times 10^{-3}$	565 ± 237
$^{13}CH_3OH$	8	329 – 653	130 ± 26[d]	$2.0 \pm 0.7 \times 10^{17}$		$1.5 \pm 0.6 \times 10^{-2}$	65 ± 27
CH_2DOH	24	61 – 896	130 ± 26	$1.1 \pm 0.3 \times 10^{18}$		$8.3 \pm 3.6 \times 10^{-2}$	2.8 ± 0.4 %
CH_3OD	6	104 – 288	130 ± 26[e]	$2.8 \pm 0.8 \times 10^{17}$		$2.2 \pm 0.9 \times 10^{-2}$	2.2 ± 0.9 %
CH_3OCHO[†]	159	86 – 693	115 ± 23	$2.7 \pm 0.8 \times 10^{17}$	$2.1 \pm 0.9 \times 10^{-2}$		
$CH_3O^{13}CHO$	6	255 – 308	115 ± 23⋆	$3.6 \pm 1.1 \times 10^{15}$		$1.3 \pm 0.5 \times 10^{-2}$	75 ± 32
CH_2DOCHO[†]	82	62 – 417	115 ± 23	$2.3 \pm 0.7 \times 10^{16}$		$8.5 \pm 3.6 \times 10^{-2}$	2.8 ± 0.4 %
CH_3OCDO[†]	3	282 – 369	115 ± 23	$4.5 \pm 1.3 \times 10^{16}$		$1.7 \pm 0.7 \times 10^{-2}$	1.7 ± 0.7 %
CHD_2OCHO[†]	5	266 – 319	115 ± 23	$5.3 \pm 1.6 \times 10^{15}$		$2.0 \pm 0.8 \times 10^{-2}$	8.2 ± 0.6 %
CH_3OCH_3	7	122 – 662	100 ± 20	$5.2 \pm 1.6 \times 10^{17}$	$4.0 \pm 1.7 \times 10^{-2}$		
$CH_3O^{13}CH_3$	11	47 – 234	100 ± 20	$1.2 \pm 0.4 \times 10^{16}$		$2.3 \pm 1.0 \times 10^{-2}$	86 ± 18
s-CH_2DOCH_3	10	46 – 337	100 ± 20	$2.4 \pm 0.7 \times 10^{16}$		$4.6 \pm 1.9 \times 10^{-2}$	2.3 ± 0.5 %
a-CH_2DOCH_3	20	68 – 243	100 ± 20[f]	$6.4 \pm 2.0 \times 10^{16}$		$1.2 \pm 0.5 \times 10^{-1}$	3.1 ± 0.3 %
H_2CO	2	173 – (1542)	155 ± 31⋆	$1.4 \pm 0.4 \times 10^{17}$	$1.1 \pm 0.5 \times 10^{-2}$		
$H_2C^{18}O$	3	97 – 279	155 ± 31⋆	$2.1 \pm 1.0 \times 10^{14}$		$1.5 \pm 0.6 \times 10^{-3}$	667 ± 280
$H_2^{13}CO$	4	98 – 240	155 ± 31	$1.5 \pm 0.5 \times 10^{15}$		$1.1 \pm 0.5 \times 10^{-2}$	93 ± 39
$H_2C^{17}O$	4	61 – 157	155 ± 31⋆	$< 6.0 \times 10^{13}$		$< 4.3 \times 10^{-4}$	> 2333
HDCO	4	26 – 219	155 ± 31⋆	$6.9 \pm 2.1 \times 10^{15}$		$4.9 \pm 2.1 \times 10^{-2}$	2.5 ± 0.5 %
D_2CO	3	127 – 370	155 ± 31⋆	$5.8 \pm 1.7 \times 10^{15}$		$4.1 \pm 1.7 \times 10^{-2}$	20.2 ± 4.2 %
C_2H_5OH	59	72 – 453	135 ± 27	$8.0 \pm 2.4 \times 10^{16}$	$6.1 \pm 2.6 \times 10^{-3}$		
CH_3CHDOH[b]	10	55 – 198	135 ± 27[g]	$7.0 \pm 2.1 \times 10^{15}$		$8.8 \pm 3.7 \times 10^{-2}$	4.4 ± 0.9 %
CH_3CH_2OD[b]	9	48 – 192	135 ± 27⋆	$< 3.5 \times 10^{15}$		$< 4.4 \times 10^{-2}$	< 4.4 %
a-CH_2DCH_2OH[b]	9	62 – 205	135 ± 27⋆	$< 3.5 \times 10^{15}$		$< 4.4 \times 10^{-2}$	< 4.4 %
s-CH_2DCH_2OH[b]	7	48 – 199	135 ± 27⋆	$< 5.2 \times 10^{15}$		$< 6.5 \times 10^{-2}$	< 3.3 %
t-HCOOH	8	35 – 530	90 ± 18	$1.3 \pm 0.4 \times 10^{16}$	$1.0 \pm 0.4 \times 10^{-3}$		
t-H^{13}COOH	6	141 – 160	90 ± 18⋆	$< 3.3 \times 10^{14}$		$< 2.5 \times 10^{-2}$	> 39
t-DCOOH	7	147 – 225	90 ± 18⋆	$< 5.1 \times 10^{14}$		$< 3.9 \times 10^{-2}$	< 3.9 %
t-HCOOD	6	131 – 208	90 ± 18⋆	$< 2.5 \times 10^{14}$		$< 1.9 \times 10^{-2}$	< 1.9 %
CH_2CO	5	357 – 996	135 ± 27	$9.1 \pm 2.7 \times 10^{15}$	$7.0 \pm 2.9 \times 10^{-4}$		
CHDCO	8	161 – 313	135 ± 27⋆	$< 3.6 \times 10^{14}$		$< 4.0 \times 10^{-2}$	< 2.0 %
HNCO	3	333 – 794	180 ± 36	$1.5 \pm 0.5 \times 10^{16}$	$1.2 \pm 0.5 \times 10^{-3}$		
DNCO	5	51 – 366	180 ± 36⋆	$< 2.5 \times 10^{14}$		$< 1.7 \times 10^{-2}$	< 1.7 %
CH_3CHO	20	153 – 385	140 ± 28	$3.5 \pm 1.1 \times 10^{15}$	$2.7 \pm 1.1 \times 10^{-4}$		
c-C_2H_4O	7	43 – 376	95 ± 19	$6.9 \pm 2.1 \times 10^{15}$	$5.3 \pm 2.2 \times 10^{-4}$		
CH_3COCH_3	85	80 – 322	125 ± 25	$2.4 \pm 0.7 \times 10^{16}$	$1.8 \pm 0.8 \times 10^{-3}$		
CH_3COOH	17	129 – 407	110 ± 22	$4.5 \pm 1.4 \times 10^{15}$	$3.5 \pm 1.5 \times 10^{-4}$		
$CH_2(OH)CHO$	9	80 – 323	155 ± 31	$1.3 \pm 0.4 \times 10^{15}$	$1.0 \pm 0.4 \times 10^{-4}$		
NH_2CHO	8	151 – 453	145 ± 29	$1.9 \pm 0.6 \times 10^{15}$	$1.5 \pm 0.6 \times 10^{-4}$		
aGg'-$(CH_2OH)_2$	20	108 – 363	145 ± 29	$4.4 \pm 1.3 \times 10^{15}$	$3.4 \pm 1.4 \times 10^{-4}$		
gGg'-$(CH_2OH)_2$	12	97 – 115	145 ± 29⋆	$< 4.8 \times 10^{15}$	$< 3.7 \times 10^{-4}$		
C_2H_5CHO	3	297 – 330	120 ± 24	$< 1.2 \times 10^{15}$	$< 9.2 \times 10^{-5}$		

Notes. [(a)] The D/H ratio, including statistics correction, is expressed in %, whereas other isotopic ratios correspond to $^{12}C/^{13}C$ or $^{16}O/^{18}O$. [(b)] Abundances of C_2H_5OH isotopologues were derived using the anti conformer entries and corrected to take the gauche conformer into account (see spectroscopic data section in Appendix C). [(c)] T_{rot} converged to 105 K and $N_{tot} = 2.2 \pm 0.7 \times 10^{16}$ cm^{-2}. [(d)] T_{rot} converged to 120 K and $N_{tot} = 2.3 \pm 0.7 \times 10^{17}$ cm^{-2}. [(e)] T_{rot} converged to 105 K and $N_{tot} = 3.4 \pm 0.7 \times 10^{17}$ cm^{-2}. [(f)] T_{rot} converged to 115 K and $N_{tot} = 6.6 \pm 2.0 \times 10^{16}$ cm^{-2}. [(g)] T_{rot} converged to 125 K and $N_{tot} = 6.6 \pm 2.0 \times 10^{15}$ cm^{-2}. [(c-g)] The rotational temperature of the main isotopologue was used to derive the column density, despite the convergence to a slightly different T_{rot}. [(⋆)] The rotational temperature did not converge; the main isotopologue value is assumed. [(†)] Manigand et al. (2018).

3. Results

In total, 15 different species as well as 16 isotopologues, have been securely detected, while 11 additional species and isotopologues are tentatively identified towards IRAS 16293A. Table 1 shows the result of the LTE analysis with the number of lines taken into account in the minimisation, the best-fit parameters (i.e. T_{rot}, N_{tot}, and Δv_{FWHM}), the abundance with respect to the main isotopologue for the same species, and the corresponding isotopic ratio.

3.1. Abundances and rotational temperatures

The relative abundances of the oxygen species are determined from their column density relative to the column density of CH_3OH. We note that H_2 was not used as a reference for the estimation of the abundances because only the lower limit of H_2 column density can be determined from the optically thick dust emission. Calcutt et al. (2018b) and Jørgensen et al. (2016) estimated the lower limit of H_2 column density towards IRAS16293A and B, respectively. The D/H ratio is based on the column density ratio and is corrected from the statistics of H atoms in the deuterated chemical group of the molecule. For example, the column density ratio of CH_2DOH is three times higher than its D/H ratio. In addition, the statistical correction includes the symmetries in the sense of the rotational spectroscopy. For example, the asymmetric deuterated dimethyl ether (a-CH_2DOCH_3) has four possible sites where the D atom could be placed, that is, out of the C–O–C plane, regardless of the rotational emission of the molecule. Thus, its column density ratio is four times higher than the D/H ratio. Similarly, the symmetric s-CH_2DOCH_3 conformer has two in-plane possible sites for the D atom, which leads to a factor of two between the column density ratio and the D/H ratio. The rotational temperature of the isotopologues was fixed to the value derived for their main isotopologue, except for formaldehyde (H_2CO) where only the $H_2^{13}CO$ rotational temperature could be constrained. For several isotopologues, the fit converged to a different rotational temperature as the main isotopologue. The difference is lower than the uncertainty for the rotational temperature and does not significantly affect the column density. The results of the minimisation for these species are indicated in the notes of Table 1. Despite the large frequency range of the survey, H_2CO isotopologues only have a few lines in the range, and most of them are either optically thick or the transition levels are not populated at all (E_{up} > 1000 K). The rotational temperature was derived using two optically thin lines of $H_2^{13}CO$, with upper state energies of 98 and 240 K. The optically thin lines, which were used to derive the column density of the other isotopologue, are the same lines used by Persson et al. (2018) in the analysis of IRAS 16293B.

Similar to the study of IRAS 16293B (Jørgensen et al. 2018), a large number of rarer isotopologues were also identified towards IRAS 16293A. We note that $CH_3^{18}OH$ and $H_2C^{18}O$ show a $^{16}O/^{18}O$ ratio close to the local interstellar medium value of 557±30 (Wilson 1999). The upper limit column density of $H_2C^{17}O$ is consistent with the canonical $^{16}O/^{17}O$ ratio of 2005 ± 155 (Penzias 1981; Wilson 1999). The ^{13}C-isotopologues that were detected do not show any significant deviation from the local ISM $^{12}C/^{13}C$ ratio of 68±15 (Milam et al. 2005). Lower $^{12}C/^{13}C$ ratios have been reported towards IRAS 16293B (Jørgensen et al. 2018) and were interpreted by a chemical process that is similar to the deuteration enhancement on the ice grain surface, which occurs during the pre-stellar formation stage. However, the mean $^{12}C/^{13}C$ ratio of 76±12 towards IRAS 16293A is consistent with the local ISM value, which indicates that the isotopic enhancement mechanism observed in IRAS 16293B does not occur in IRAS 16293A. Deuterated isotopologues of CH_3OH, H_2CO, C_2H_5OH, dimethyl ether (CH_3OCH_3), CH_3OCHO, CH_2CO, HCOOH, and isocyanic acid (HNCO) are present in the gas with D/H ratios of 2–5%. As it was observed towards IRAS 16293B (Persson et al. 2018; Manigand et al. 2018), the doubly-deuterated isotopologues D_2CO and CHD_2OCHO are significantly enhanced compared to the singly-deuterated isotopologues. The implications are discussed in the next section of the paper.

New spectroscopic data for deuterated CH_3CHO isotopologues were recently reported by Coudert et al. (2019) who add information about CH_2DCHO to that of CH_3CDO from Elkeurti et al. (2010), which was utilised for the first detection reported by Jørgensen et al. (2018). To test their experimental results, Coudert et al. used the new spectroscopic data to search for CH_2DCHO and CH_3CDO in the PILS dataset. They report the presence of 93 and 43 transitions of CH_2DCHO and CH_3CDO across a 10 GHz frequency range, respectively, and they made rough estimates of the column densities based on the archival 12m array PILS data only. In order to carry out a consistent comparison of the PILS results in terms of assumptions concerning analysed positions, source sizes, velocity shift, and FWHM as well as using the combined 12m+ACA dataset, we analysed the data for those isotopologues with the same methodology in this paper as the other PILS papers. The derived column density and rotational temperature are reported in Table 2. The new column density reported for CH_3CDO is consistent with the value that was derived in the previous study of Jørgensen et al. (2018).

3.2. New detections

In addition to the 31 identified isotopologues towards IRAS 16293A, two new species, CH_3OCH_2OH and t-$C_2H_5OCH_3$, were detected towards IRAS 16293B, exclusively. Only an upper limit column density was derived for the two species towards IRAS 16293A, assuming the same rotational temperature as for IRAS 16293B. Column densities, relative abundances to CH_3OH, and upper limits are reported in Table 2. Both species have already been detected in the ISM before; however, this is the first time they were detected in a low mass star-forming region. McGuire et al. (2017) report the detection of CH_3OCH_2OH towards the high-mass protostellar core NGC 6334I MM1, with a relative abundance of ∼0.03 with respect to CH_3OH. This abundance is significantly higher than those towards IRAS 16293A and IRAS 16293B and this is discussed in the next section along with the other O-bearing species. We note that t-$C_2H_5OCH_3$ was tentatively detected in several high-mass sources, such as W51 e1/e2 (Fuchs et al. 2005), which was refuted by Carroll et al. (2015) and Orion KL (Tercero et al. 2015). Later, Tercero, B. et al. (2018) confirmed the detection towards the Orion KL compact bridge region. The last study reported a rotational temperature of 150±20 K and a column density of $3.0 \pm 0.9 \times 10^{15}$ cm^{-2}, leading to an abundance of 3.7×10^{-9} with respect to H_2. This estimation is consistent with the abundance derived towards IRAS 16293A and B.

3.3. Identification of CHD_2OH lines

Thirty-one lines of CHD_2OH were found in the range of the observations. CHD_2OH has already been detected at lower frequencies towards IRAS 16293 (Parise et al. 2002) using the IRAM 30-metre telescope. At the present day, only a small number of lines are publicly available in terms of spectroscopic data, including the line strength values, although, more extended frequency lists can be found in the literature (e.g. Ndao et al. 2016; Mukhopadhyay 2016). Therefore, this species requires special treatment.

To confirm the identification CHD_2OH in spectrum, each line was independently fitted to a simple Gaussian line profile in terms of amplitude and by using the same velocity peak v_{lsr} and FWHM as CH_3OH, that is, 0.8 and 2.2 km s^{-1} as well as 2.7 and 1.0 km s^{-1} for IRAS 16293A and IRAS 16293B, respec-

Table 2: Rotational temperature, column density, and relative abundance with respect to CH_3OH for the newly detected species.

Species	IRAS 16293B		
	T_{rot} (K)	N_{tot} (cm^{-2})	N_{tot} / N_{CH_3OH}
t-$C_2H_5OCH_3$	100	$1.8 \pm 0.2 \times 10^{16}$	1.8×10^{-3}
CH_3OCH_2OH	130	$1.4 \pm 0.2 \times 10^{17}$	1.4×10^{-2}
$CH_3CDO^{\dagger}$	125*	$7.4 \pm 0.7 \times 10^{15}$	7.4×10^{-4}
$CH_2DCHO^{\dagger}$	125*	$6.2 \pm 0.6 \times 10^{15}$	6.2×10^{-4}
Species	IRAS 16293A		
	T_{rot} (K)	N_{tot} (cm^{-2})	N_{tot} / N_{CH_3OH}
t-$C_2H_5OCH_3$	100**	$< 2.7 \times 10^{16}$	$< 2.1 \times 10^{-3}$
CH_3OCH_2OH	130**	$< 2.7 \times 10^{17}$	$< 2.1 \times 10^{-2}$
CH_3CDO	140*	$< 6.0 \times 10^{14}$	$< 4.6 \times 10^{-5}$
CH_2DCHO	140*	$< 6.0 \times 10^{14}$	$< 4.6 \times 10^{-5}$

Notes. $^{(\dagger)}$ CH_2DCHO and CH_3CDO were initially reported in Coudert et al. (2019). $^{(\star)}$ The rotational temperature is assumed to be the same as the main isotopologue, which is 100 and 125 K for IRAS 16293A and IRAS 16293B, respectively (Lykke et al. 2017). $^{(\star\star)}$ The rotational temperature did not converge; the same value as IRAS 16293B is assumed.

tively. The line frequencies match 24 and 16 lines of the 31 candidates, for IRAS 16293A and B, respectively, without any hint of blending effect with other species. Figures D.1 and D.2 show the Gaussian fits of all the lines. The integrated intensity over ±FWHM around the rest frequency was derived for each unblended lines and is noted in Table D.1. The average integrated intensity of the lines assigned to CHD_2OH is higher than 0.3 Jy beam^{-1} km s^{-1} for IRAS 16293B. Also, several lines towards IRAS 16293B show a small blue-shifted absorption counterpart, which is a characteristic of infalling motions (Pineda et al. 2012), which are associated with optically thick lines. In comparison to the other detected species, especially to CH_2DOH and CH_3OH, these intensities correspond to high line opacities due to a high column density. This suggests a high abundance of CHD_2OH as well, and it is a key factor motivating further searches for CD_3OH, as was already detected by Parise et al. (2004), and CD_3OD. Despite the substantial data available on CD_3OH and CD_3OD (Mollabashi et al. 1993; Walsh et al. 1998; Xu et al. 2004; Müller et al. 2006), we did not find any line that corresponds to those of these two species in the present observations.

4. Discussion

4.1. Comparison between IRAS 16293 A and B

Most of the species and their isotopologues reported in this study are present towards both IRAS 16293A and B; however, their abundances are different in a few cases.

Figure 2 shows the abundances of the main isotopologues with respect to CH_3OH towards IRAS 16293 A and B. The column densities, from which the abundances were derived, were determined by using the spectrum extracted from the offset positions, as described in the previous section for IRAS 16293A, which were used in previous studies of IRAS 16293B (Coutens et al. 2016; Lykke et al. 2017; Jørgensen et al. 2016). Towards IRAS 16293A, the abundances relative to CH_3OH of CH_3OCHO, ethylene oxide (c-C_2H_4O), CH_3OCH_3, CH_3COCH_3, acetic acid (CH_3COOH), and HNCO are similar to the abundance observed towards IRAS 16293B. On the other hand, the abundances of CH_2CO, H_2CO, CH_3CHO C_2H_5OH, $CH_2(OH)CHO$, $(CH_2OH)_2$, *t*-HCOOH, and formamide (NH_2CHO) are significantly lower towards IRAS 16293A than those towards IRAS 16293B. This selective differentiation could reflect the differentiation of the species across the two protostars. However, it is not possible to rule out the effects of the CH_3OH abundance with respect to H_2, for which the column density cannot be properly estimated. In addition, considering a single species as a reference for the abundance of all the species can interfere with the relation between the abundance of several species. For example, in the case of IRAS16293 and the comet 67P/Churyumov-Gerasimenko, Drozdovskaya et al. (2019) show that it is more consistent to discuss the abundance of N-bearing and S-bearing species with respect to CH_3CN and CH_3SH, respectively.

In order to complete the picture, we estimated the statistical distance S of abundance ratios of each pair of species between IRAS 16293 A and B, as detailed in Appendix A. Figure 3 shows the colour map of this cross-comparison; each cell corresponds to the statistical distance of the abundance ratio of two species towards IRAS 16293A as compared to IRAS 16293B. The advantage of this comparative analysis is that the abundances do not rely on a single species. This technique offers a global view of the comparison in terms of molecular abundance between the offset position from the two sources. The first and the tenth rows of the map are shown in the right panels of the figure and correspond to the comparison of abundances relative to CH_3OH and C_2H_5OH, respectively, towards IRAS 16293A in comparison to IRAS 16293B. The upper right panel shows a clear distinction between the similar abundance of species with respect to CH_3OH towards IRAS 16293A and B as well as those with a higher abundance towards IRAS 16293B in comparison to those towards IRAS 16293A. This separation is represented with a vertical dashed line, between CH_3OCH_3 and HNCO. A similar separation, which is located between CH_2CO and H_2CO, is shown on the lower right panel where the abundances are plotted with respect to C_2H_5OH towards IRAS 16293A in comparison to the abundances towards IRAS16293B. These separations represent a factor of two difference in the relative abundance ratio between IRAS16293A and B. This corresponds to a significance of 2σ, given the column density uncertainties.

The cross-comparison of all the main isotopologues between IRAS 16293 A and B suggests three distinct categories of species. The first category (noted Category I in Fig. 3) includes the species, such as CH_3OH, CH_3OCHO, c-C_2H_4O, CH_3COCH_3, CH_3COOH, CH_3OCH_2OH, *t*-$C_2H_5OCH_3$, and CH_3OCH_3, which have similar abundances between IRAS 16293A and B, or a low absolute statistical distance. H_2CO, CH_3CHO, $CH_2(OH)CHO$, and $(CH_2OH)_2$ show a much lower abundance with respect to all the other species. This corresponds to the righter most part of the distance map (Category III in Fig. 3). The remaining species are in an intermediate category (Category II in Fig. 3) and are characterised by a lower abundance with respect to the first category species and a higher abundance with respect to the most depleted species for IRAS 16293A in comparison to IRAS 16293B. This comparative analysis suggests that there are at least two processes that deplete some of the species towards the offset position of IRAS 16293A compared to the offset position of IRAS 16293B. The possible causes of these depletions are discussed in the following sections.

4.2. Spatial extent

The spatial distribution of the emission towards IRAS 16293 A and B can be very different depending on the species. The deconvolved source size of the IRAS 16293B continuum emission

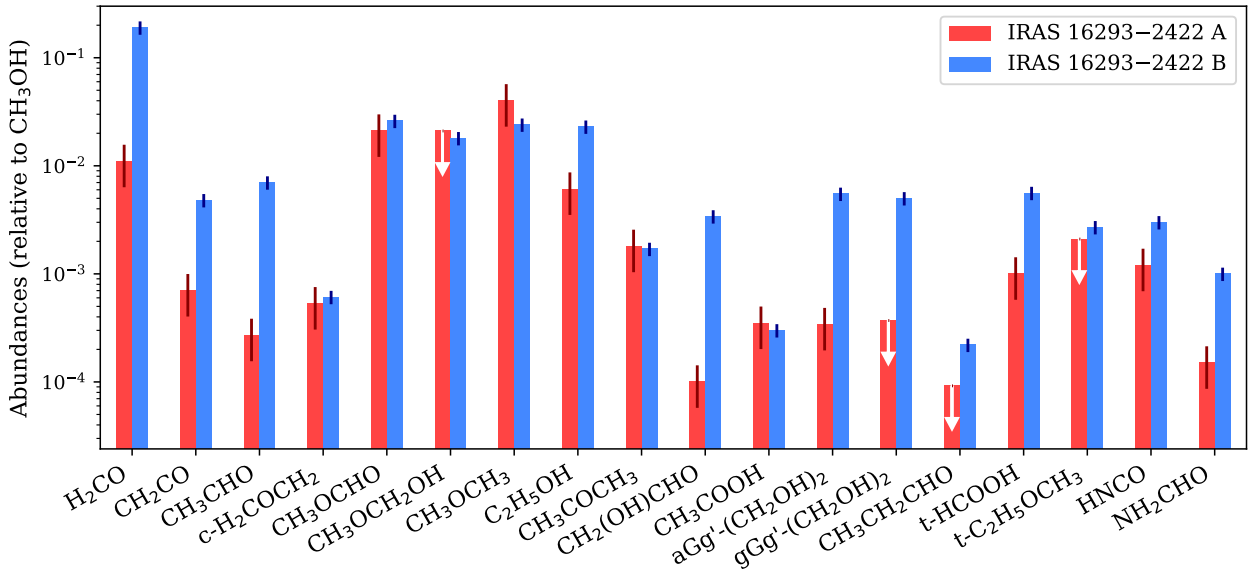


Fig. 2: Relative abundances of the main isotopologues with respect to CH_3OH, towards IRAS 16293A in red and IRAS 16293B in blue. The abundances towards IRAS 16293B are based on Persson et al. (2018) for H_2CO, Lykke et al. (2017) for CH_3CHO, c-H_2COCH_2, and CH_3COCH_3, Jørgensen et al. (2016) for $CH_2(OH)CHO$ and CH_3COOH, and Jørgensen et al. (2018) for CH_2CO, CH_3OCH_3, C_2H_5OH, CH_3OCHO, $(CH_2OH)_2$, and t-HCOOH. We note that 30% and 10% of the uncertainties on the column density are considered for IRAS 16293A and IRAS 16293B, respectively.

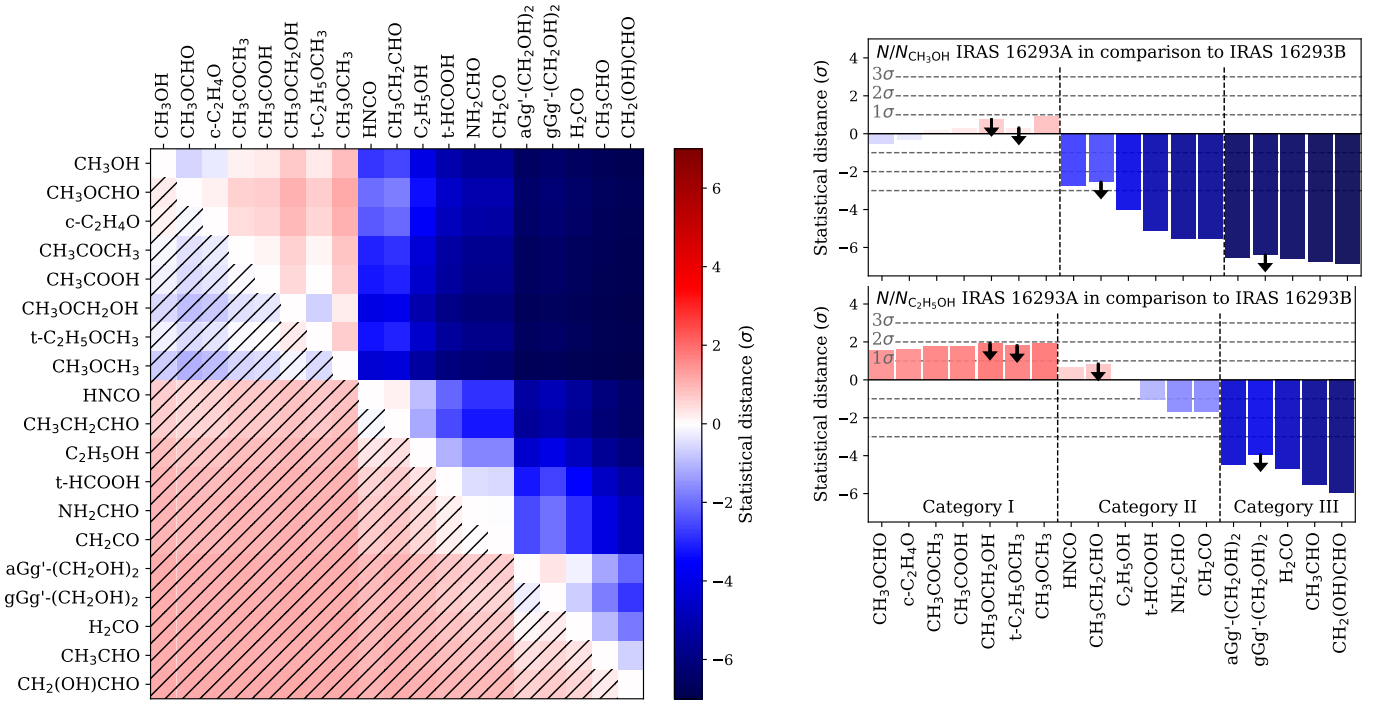


Fig. 3: (*left*) Cross-comparison of species from IRAS 16293A in comparison to those from IRAS 16293B. The statistical distance S is represented in the colour scale for each pair of species. One cell with a given value S of the plot should be read as 'The abundance of the species X with respect to Y towards IRAS 16293A is S sigma higher or lower compared to IRAS 16293B', with X and Y species taken from the X-axis and Y-axis, respectively. A positive value of S corresponds to N_X/N_Y higher in IRAS 16293A in comparison to IRAS 16293B. (*right*) 'CH_3OH' and 'C_2H_5OH' rows of the cross-comparison map. The two plots show the comparison of abundances with respect to CH_3OH (upper panel) and C_2H_5OH (lower panel) towards IRAS 16293A and IRAS 16293B in terms of statistical distance.

is estimated to be 0″.5 (Jørgensen et al. 2016), which is similar to the beam size of the observations. Most of the detected species roughly follow the same distribution as the continuum and have the same source size. Concerning IRAS 16293A, the continuum emission, as well as the molecular line emission arising from the gas, is more extended in the NE-SW axis where a 6 km s^{-1} veloc-

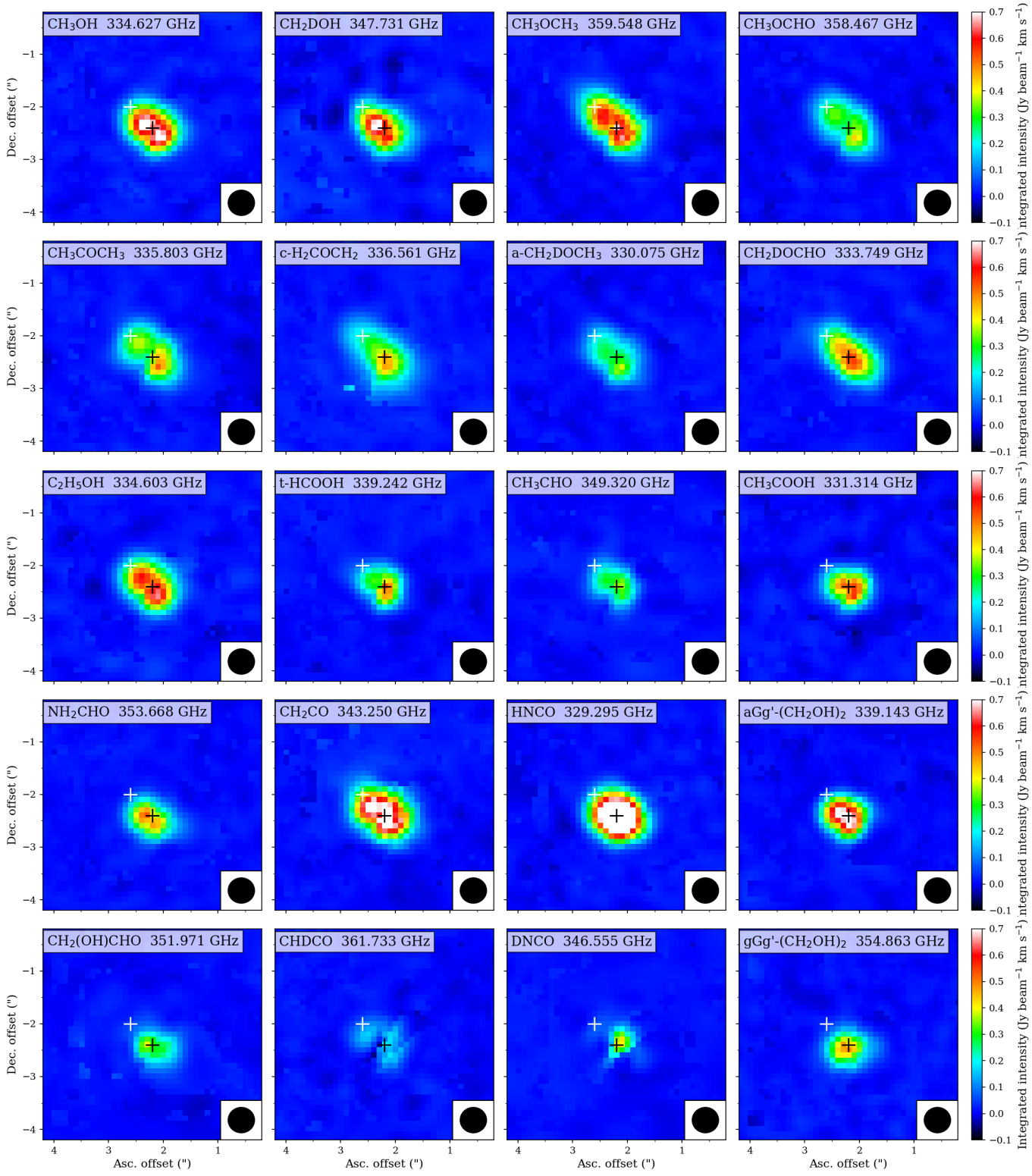


Fig. 4: Representative velocity integrated emission maps of the detected COMs towards IRAS16293A. The black and white crosses indicate the continuum peak position and the offset position, respectively. The species and the line frequency are noted in the top-left corner and the 0″.5 beam is shown in the bottom right corner of each panels.

ity gradient was reported (Pineda et al. 2012; Favre et al. 2014; Jørgensen et al. 2016; Oya et al. 2016). Small variations in the spatial distribution of different species towards IRAS 16293A can be marginally resolved with the beam of PILS observations. However, the velocity gradient, which is associated with the very high line density that is present in the spectrum, makes it very difficult to integrate a single line across the source without contamination from nearby lines of other species.

Calcutt et al. (2018b) developed a new method to map the emission, called the velocity integrated emission map (VINE

map), which takes into account the velocity shift of the emitting gas when integrating over the molecular emission. At each pixel, the integration range is then shifted to the peak velocity of the line to be mapped. When there is no large velocity variation across the map, which is the case for IRAS 16293B for instance, the VINE map is equivalent to the standard integrated emission map (moment zero map). For IRAS 16293A, the velocity shift correction at each pixel of the VINE maps is based on the same bright transition $7_{3,5} - 6_{4,4}$ of CH_3OH at 337.519 GHz as used by Calcutt et al. (2018b). This transition is particularly suited for tracing the hot corino while being well isolated from other lines. Figure 4 shows VINE maps of the main isotopologues, and few deuterated conformers were detected towards IRAS 16293A. In this study, the VINE maps were only used to check whether the emission distribution reaches the offset position, where we analysed the spectrum, as indicated by the white cross.

The emission of the species that have similar abundances towards IRAS 16293A and B is distributed along the velocity gradient direction and cover the offset position, whereas the emission distribution of the depleted species towards IRAS 16293A in comparison to IRAS 16293B is located around the continuum peak position of the respective sources and does not show the elliptical distribution of the continuum emission towards IRAS 16293A. Only the CH_3COOH emission distribution is as compact as the $(CH_2OH)_2$ emission distribution, while the abundance towards IRAS 16293A and B are similar. We checked the distribution emission towards IRAS 16293B as well as for this species and noticed that the emission does not cover the offset position used in the previous studies. Therefore, CH_3COOH seems depleted towards both IRAS 16293A and B. This is why CH_3COOH does not show a difference between IRAS 16293A and B since it belongs to the most compact region of the warm envelope.

Spatial differences between COMs were previously observed towards the Galactic Centre Sgr B2 region (Hollis et al. 2001) as well as towards high-mass protostars (for example, Calcutt et al. 2014). Hollis et al. observed the emission of CH_3OCHO and $CH_2(OH)CHO$, among others, at two different angular resolutions. They detected the two species with an ∼60" beam size using the NRAO 12 m telescope, whereas the Berkeley-Illinois-Maryland Association (BIMA) observations with a beam of ∼5" only revealed CH_3OCHO. They suggested that $CH_2(OH)CHO$ was much more extended compared to CH_3OCHO and its emission was spatially filtered by the interferometric character of the observations. These findings are supported by the more recent study of Li et al. (2017) towards an extended region of the Galactic Centre in which the authors reported cold gas emission of $CH_2(OH)CHO$ ∼36 pc in width around Sgr B2(N). We note that, these two observations of the $CH_2(OH)CHO$ spatial extent are specific to the Galactic Centre, where non-thermal desorption processes put the $CH_2(OH)CHO$ in the gas phase at temperatures much lower than the thermal desorption temperature of this species.

Xue et al. (2019) consistently observed the three isomers CH_3COOH, CH_3OCHO, and $CH_2(OH)CHO$ towards Sgr B2(N) using ALMA in Band 3 with an angular resolution of 1.″6, which is sufficient to resolve the sources. The spatial distribution of the species reveals that CH_3OCHO is more extended than both $CH_2(OH)CHO$ and CH_3COOH, which is in agreement with the present study. Xue et al. suggest that the different formation pathways of the tree species through ice surfaces and gas-phase chemistry could explain the spatial differentiation. This interpretation was supported by the correlation with the distribution of the respective precursors especially for gas-phase formation, such as CH_3OCH_3, which is the precursor of CH_3OCHO (Balucani et al. 2015), and C_2H_5OH the precursor of $CH_2(OH)CHO$ and CH_3COOH (Skouteris et al. 2018). The search for precursors through ice surfaces formation pathway is limited by the current infra-red absorption observations. Alternatively, the authors suggest that the effective desorption temperature of the species could explain their spatial distribution difference based on temperature-programmed desorption (TPD) experiments of $C_2H_4O_2$ isomers (Burke et al. 2015). During the TPD, CH_3OCHO desorbed at ∼70 K whereas $CH_2(OH)CHO$ and CH_3COOH were released in the gas phase at ∼110 K. In the warm-up model of star formation, this would result in a more extended emission of CH_3OCHO in comparison to the two other isomers.

Calcutt et al. (2014) simultaneously detected CH_3OCHO and $CH_2(OH)CHO$, among other species, towards three high-mass sources, G31.41+0.31, G29.96–0.02, and G24.78+0.08A, which are located at 3.5, 7.1, and 7.7 kpc away, respectively. They find that CH_3OCHO was more extended than $CH_2(OH)CHO$ towards G31 and that the two species had the same extent towards the two other sources. The spatial differentiation found in G31 could be similar to IRAS 16293; however, $CH_2(OH)CHO$ and the other depleted species towards IRAS 16293A could also trace a deeper region in the envelope due to the excitation conditions. For example, CH_3OCHO lines are optically thicker than those of $CH_2(OH)CHO$ and show a more extended spatial distribution.

Also, such a spatial differentiation can be inferred indirectly. The first detection of glycolaldehyde by Jørgensen et al. (2012) was performed with ALMA at ∼2" angular resolution: This is enough to separate the two components of the binary system but larger than the source size of both components. Jørgensen et al. find a relative abundance $CH_3OCHO/CH_2(OH)CHO$ of 10-15 for both protostars on these scales and did not see the same evidence for depletion of $CH_2(OH)CHO$ with respect to CH_3OCHO for IRAS 16293A in comparison to IRAS 16293B, as discussed above. However, it is consistent with the interpretation that $CH_2(OH)CHO$, as well as the other most depleted species towards the offset position from IRAS 16293A, are located in a more compact region of the hot corino. This is also supported by observations of other COMs, such as CH_3OCH_3, D_2CO (Jørgensen et al. 2011), and C_2H_5OH (Bisschop et al. 2008).

4.3. Differentiation in rotational temperature

The distribution of COMs towards IRAS 16293A suggests that a significant part of the emission is missing at the extracted spectrum position. However, the estimation of the rotational temperature is sensitive to the intensity variation of one line with respect to another line with a different upper energy level. Thus, the derivation of the rotational temperature is not affected by the apparent depletion due to the spatial extent and can be securely compared species-to-species.

Towards IRAS 16293A, the rotational temperatures of the detected species and their isotopologues are between 90 and 180 K, where HNCO, H_2CO, $CH_2(OH)CHO$, $(CH_2OH)_2$, NH_2CHO, CH_3CHO, and C_2H_5OH are the hottest species. Although the distinction between those hot species and the other species is not pronounced, the hot species seem to be located closer to the protostars compared to the other species, showing a lower rotational temperature.

Using the PILS observations towards IRAS 16293B, Jørgensen et al. (2018) detected the same species as those pre-

sented in this study and derived their rotational temperature. The authors find that the species located in the hot corino could be distinguished into two groups depending on their rotational temperature. Species such as CH_3OH, C_2H_5OH, CH_3OCHO, NH_2CHO, HNCO, $CH_2(OH)CHO$, and $(CH_2OH)_2$ were observed with an rotational temperature of 250–300 K, whereas CH_2CO, CH_3CHO, CH_3OCH_3, H_2CO, and c-H_2COCH_2 were found at 100–150 K. Using these results and the previous results of PILS observations towards IRAS 16293B from Coutens et al. (2016); Jørgensen et al. (2016) and Persson et al. (2018), Jørgensen et al. find a correlation between the rotational temperature and the desorption temperature of the oxygen-bearing COMs that are thought to mainly form on ice surfaces. This implies that the species that have a high rotational temperature (250–300 K) are more predominantly located in the hot and compact region of the hot corino, while the lower rotational temperature species belong to a more extended region inside the hot corino (see Fig. 4 of Jørgensen et al. 2018). By comparing this scenario to the difference in the spatial extent observed in IRAS 16293A, the compact species, such as $CH_2(OH)CHO$, $(CH_2OH)_2$, NH_2CHO, HNCO, and C_2H_5OH, are associated with high rotational temperature, whereas extended species, such as c-H_2COCH_2, CH_3OCH_3, and CH_3COCH_3, have a low rotational temperature. The ordering of the species across the onion-like structure of the envelope is in agreement with the desorption temperatures observed in temperature-programmed desorption (TPD) experiments of pure and mixed ices (Öberg et al. 2009; Fedoseev et al. 2015a,b, 2017; Paardekooper et al. 2016; Chuang et al. 2016; Qasim et al. 2019a,b).

In addition, the rotational temperature of CH_3COOH towards IRAS 16293B is consistent with its most compact location in the envelope of both sources. However, the correlation between the rotational temperature and the location does not work in IRAS 16293A for CH_3OH, CH_3OCHO, CH_2CO, H_2CO, CH_3CHO, and *t*-HCOOH.

Concerning CH_3OH and CH_3OCHO, these two species were found to be hot species in IRAS 16293B; however, they correspond to cold and extended species in IRAS 16293A. Their optically thick lines suggest the presence of two components towards IRAS 16293B that are indistinguishable due to the smaller source size with respect to the angular resolution: one is at a rotational temperature of 300 and another is at ∼125 K (Jørgensen et al. 2018). In addition, the rotational temperature derived towards IRAS 16293A for the same two species is only consistent with the second component at 125 K, indicating that the bulk of the emission consists of the extended warm gas. From this, CH_3OH and CH_3OCHO are found to trace not only the central core but also the extended part of the hot corino.

Regarding CH_2CO isotopologues, there are only a few lines in the range of the observations and most of those are blended with small species, such as ^{33}SO at ∼343.08 GHz and CS at ∼342.88 GHz. The deuterated isotopologue CHDCO suggests that the low abundance towards IRAS 16293A compared to IRAS 16293B is due to the spatial extent differences between the two sources. The emission distribution of H_2CO was found to be much more complex and extended across the binary protostars and it traces both the hot corino region and the outflow interface with the bridge structure between IRAS 16293A and B and the E-W outflow emerging from IRAS 16293A (van der Wiel et al. 2019).

The few unblended, but optically thick, lines of CH_3CHO show a large distribution towards both sources, suggesting that the bulk of the emission corresponds to the extended part of the hot corino, despite the abundance difference between sources A and B. The three-phase chemical model of Garrod (2013) shows that the abundance of CH_3CHO in the gas phase increases during the evolution of the hot corino, which occurs even before the species desorbs from the ice grain surfaces. This suggests that gas-phase formation paths significantly contribute to the formation of CH_3CHO at relatively low temperatures before the bulk of the species desorb from the ice. Concerning the abundance observed towards IRAS 16293 binary, if the gas-phase formation paths effectively produce CH_3CHO in the outer part of the hot corino, it should increase the abundance of CH_3CHO towards the most luminous source with respect to the other component. However, the luminosity of IRAS 16293A was estimated to be ∼ 18 $L_\odot$, which is six times higher than IRAS 16293B (Jacobsen et al. 2018).

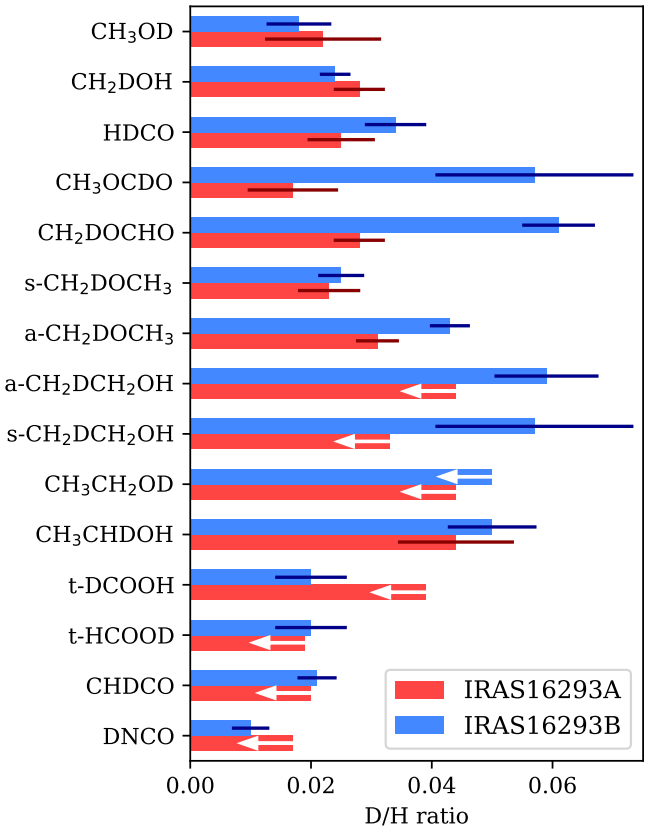


Fig. 5: D/H ratio of the deuterated species detected towards IRAS 16293A in red and IRAS 16293B in blue. The D/H ratio is calculated from the abundance ratio, with the statistical correction due to the chemical group (see Appendix B of Manigand et al. 2018). D/H ratios towards IRAS 16293B are taken from Coutens et al. (2016), Lykke et al. (2017), Persson et al. (2018) and Jørgensen et al. (2018).

In summary, the analysis of the spatial extent, the abundances, and the rotational temperatures suggests that the hot corinos show a stratification of the COMs along the distance to the forming star. This spatial differentiation towards IRAS 16293A could be linked to the rotational temperature of the species observed towards IRAS 16293B in the way that species at 300 K are more compact than the species at 125 K. Although this spatial differentiation is not resolved for IRAS 16293B, the rotational temperature suggests its presence. Towards IRAS 16293A, the difference in rotational temperature between com-

pact and extended species is less pronounced, which could be due to the geometry of the source (inclination, size) or the presence of the nearly edge-on disc (Pineda et al. 2012; Favre et al. 2014; Girart et al. 2014).

4.4. D/H ratio

The sensitivity of the ALMA observations makes the detection of many deuterated isotopologues of the oxygen-bearing species possible. Figure 5 compares the D/H ratios of these species derived from the estimated column densities found towards the offset position of IRAS 16293A and reported in the previous studies of IRAS 16293B (Coutens et al. 2016; Lykke et al. 2017; Persson et al. 2018; Jørgensen et al. 2018) on a linear scale. In general, the D/H ratios of IRAS 16293A species are found to be as high as those of the species of IRAS 16293B. However, due to the higher uncertainty in the column densities and the higher number of upper limits, it is difficult to observe a trend in the deuteration itself. Nevertheless, there is apparently no direct correlation between the D/H ratios and the stratification suggested by the rotational temperatures. This could suggest that contrary to the rotational temperatures and the spatial extents, which give a clue as to the structure of the hot corino and thus the warm chemistry in situ, the D/H ratio gives information about the history of the envelope during the pre-stellar phase when the gas was cold enough to let the D/H ratio of the frozen species increase. This is supported by the D/H ratio of the doubly-deuterated isotopologues D_2CO of $2.0 \pm 0.4 \times 10^{-1}$ and CHD_2OCHO of $8.2 \pm 0.6 \times 10^{-2}$ (Manigand et al. 2018) found towards IRAS 16293A.

Using the result reported in Table 2 and the column density of CH_3CHO measured towards IRAS16293B (Lykke et al. 2017; Jørgensen et al. 2018), which is 1.2×10^{17} cm^{-2}, the D/H ratio of CH_2DCHO and CH_3CDO are 1.4 and 4.7%, respectively. The upper limits of the D/H ratio of CH_2DCHO and CH_3CDO towards IRAS 16293A are < 6 and < 17%, respectively. The D/H ratio of the groups CH_3– and HCO– are significantly different for CH_3CHO even after applying the statistical correction for both sources. Assuming that the main formation route is due to the addition of those two radicals on the ice surface during the warm-up phase, then the difference in deuteration may indicate that the deuteration enhancement is different for CH_3 and HCO, which are already in the prestellar phase when the temperature is low enough to favour the deuteration enhancement of H_3^+ in the gas phase. However, the other species thought to be formed on ice surfaces do not show such a difference in the D/H ratio between CH_3– or CH_2– and HCO– groups, such as CH_3OCHO and $CH_2(OH)CHO$ (Jørgensen et al. 2016). This suggests a selective process, independent of the luminosity difference between IRAS 16293A and B, which increases the deuteration of HCO– or decreases those of CH_3– without significantly impacting the other species.

As a side note, the high intensity of the candidate lines found for CHD_2OH in the range of the observations and the enhancement of the D/H ratio of the two doubly-deuterated isotopologues D_2CO and CHD_2OCHO with respect to their respective singly-deuterated isotopologues, HDCO and CH_2DOCHO, suggest a roughly equally high column density for CHD_2OH. This stresses the importance of future studies on the spectroscopy of CHD_2OH and even more its deuterated conformers CD_3OH and CD_3OD.

5. Conclusions

In this study, we analysed the molecular content of the protostar IRAS 16293A at the hot corino scale and compared the abundances to those measured towards its protostar companion IRAS 16293B. Numerous O-bearing species have been detected, along with their rarer isotopologues. The main findings of this work are summarised below.

1. The abundances with respect to CH_3OH of half of the species are significantly lower towards the 0″.6 offset position from IRAS 16293A in comparison to the 0″.5 offset position from IRAS 16293B in spite of its higher luminosity.
2. The cross-correlation of the main isotopologue abundances highlights a selective differentiation depending on the species observed. Different categories are identified whether the species abundances are similar or significantly different between IRAS 16293A and B.
3. The first category, including CH_3OH, CH_3OCHO, c-C_2H_4O, CH_3COCH_3, CH_3COOH, CH_3OCH_3, *t*-$C_2H_5OCH_3$, and CH_3OCH_2OH, corresponds to the species that have a similar abundance towards both IRAS 16293A and B. These species show an extended spatial distribution across IRAS 16293A and have a relatively low rotational temperature of ∼125 K towards IRAS 16293B, except for CH_3COOH, CH_3OH and CH_3OCHO. CH_3COOH spatial distribution is much more compact towards both IRAS 16293A and B than the other extended species and the rotational temperature found towards IRAS 16293B, which is unambiguously ∼300 K. In addition, CH_3OH and CH_3OCHO show attributes of both compact and extended regions as suggested by their extended distribution and their high desorption temperature. Their emission is suspected to trace both regions in the hot corino.
4. The second category concerns the species showing a significantly lower abundance towards IRAS 16293A with respect to IRAS 16293B, which are HNCO, C_2H_5CHO, C_2H_5OH, *t*-HCOOH, NH_2CHO, CH_2CO, H_2CO, CH_3CHO, $CH_2(OH)CHO$, and $(CH_2OH)_2$. These species have a more compact spatial distribution towards IRAS 16293A compared to the first category of species. In addition, they tend to have a high rotational temperature of∼300 K, especially for those that are the most compact, such as $CH_2(OH)CHO$ and $(CH_2OH)_2$. However, the spatial distribution difference is not resolved towards IRAS 16293B, the rotational temperature difference between compact and extended species is more pronounced though. H_2CO, CH_2CO, and CH_3CHO do not fit into any category as they have a roughly compact spatial emission but a low rotational temperature.
5. In the search for O-bearing species, we report the new detection of *t*-$C_2H_5OCH_3$ and CH_3OCH_2OH towards IRAS 16293B. Their abundances with respect to CH_3OH are consistent with the previous detection of these species towards the high mass protostellar regions Sgr B2(N) and Orion KL. Upper limits of their column density are derived towards IRAS 16293A.
6. The D/H ratio is not correlated to the structure of the hot corino itself; however, it is the result of what happens during the formation of COMs in the pre-stellar phase. The multiply-deuterated COMs seem to have a systematically higher D/H ratio compared to singly-deuterated species. More observations of different sources, supported by future spectroscopic studies of other multiply-deuterated COMs, are required to confirm this trend. In addition, we report the identification of 23 CHD_2OH transitions at 0.8 mm wavelength, which have not been observed so far. The intensity

of CHD_2OH lines suggests a high abundance and D/H ratio, as it is for CHD_2OCHO. The identification of these CHD_2OH transitions highlights the need for spectroscopic data for CHD_2OH and CD_3OH to derive their rotational temperatures and their column densities and to get their D/H ratios.

As discussed in this paper, abundance variations between IRAS 16293A and B suggest that the spatial distributions are different for the species associated with low or high rotational temperatures. Whether the origins of these differences are physical or chemical, future higher angular observations will be critical in resolving the innermost structure of the two protostars.

Acknowledgements. The authors wish to thank the anonymous referee for the constructive comments that significantly improved the paper. The authors are grateful to Brett McGuire and Roman Motiyenko for providing the line strengths of CH_3OCH_2OH spectroscopic data. The authors acknowledge Gleb Fedoseev for the valuable discussion about the desorption temperatures from the TPD experiments of the O-bearing COMs and Troels C. Petersen for discussions of the statistical methods. This paper makes use of the following ALMA data: ADS/JAO.ALMA#2012.1.00712.S and ADS/JAO.ALMA#2013.1.00278.S. ALMA is a partnership of ESO (representing its member states), NSF (USA) and NINS (Japan), together with NRC (Canada), NSC and ASIAA (Taiwan), and KASI (Republic of Korea), in cooperation with the Republic of Chile. The Joint ALMA Observatory is operated by ESO, AUI/NRAO and NAOJ. The group of J.K.J. acknowledges support from the H2020 European Research Council (ERC) (grant agreement No 646908) through ERC Consolidator Grant ???S4F???. Research at Centre for Star and Planet Formation is funded by the Danish National Research Foundation. A.C. postdoctoral grant is funded by the ERC Starting Grant 3DICE (grant agreement 336474). M.N.D. is supported by the Swiss National Science Foundation (SNSF) Ambizione grant 180079, the Center for Space and Habitability (CSH) Fellowship and the IAU Gruber Foundation Fellowship. This research has made use of NASA's Astrophysics Data System and VizierR catalogue access tool, CDS, Strasbourg, France (Ochsenbein et al. 2000), as well as community-developed core Python packages for astronomy and scientific computing including Astropy (Robitaille et al. 2013), Scipy (Jones et al. 2001), Numpy (van der Walt et al. 2011) and Matplotlib (Hunter 2007).

References

Altwegg, K., Balsiger, H., Berthelier, J. J., et al. 2017, MNRAS, 469, S130
Andre, P. & Montmerle, T. 1994, ApJ, 420, 837
Auwera, J. V. 1992, J. Mol. Spectrosc., 155, 136
Bacmann, A., Taquet, V., Faure, A., Kahane, C., & Ceccarelli, C. 2012, A&A, 541, L12
Balucani, N., Ceccarelli, C., & Taquet, V. 2015, MNRAS, 449, L16
Baskakov, O. I. 1996, J. Mol. Spectrosc., 180, 266
Baskakov, O. I., Alekseev, E. A., Motiyenko, R. A., et al. 2006, J. Mol. Spectrosc., 240, 188
Baskakov, O. I., Bürger, H., & Jerzembeck, W. 1999, J. Mol. Spectrosc., 193, 33
Bellet, J., Deldalle, A., Samson, C., Stenbeckeliers, G., & Wertheimer, R. 1971, J. Mol. Struct., 9, 65
Belov, S. P., Tretyakov, M. Y., Kleiner, I., & Hougen, J. T. 1993, J. Mol. Spectrosc., 160, 61
Bergner, J. B., Öberg, K. I., Garrod, R. T., & Graninger, D. M. 2017, ApJ, 841, 120
Bisschop, S. E., Jørgensen, J. K., Bourke, T. L., Bottinelli, S., & van Dishoeck, E. F. 2008, A&A, 488, 959
Biver, N., Bockelée-Morvan, D., Debout, V., et al. 2014, A&A, 566, L5
Blake, G. A., Sutton, E. C., Masson, C. R., & Phillips, T. G. 1987, ApJ, 315, 621
Blanco, S., López, J. C., Lesarri, A., & Alonso, J. L. 2006, JACS, 128, 12111, pMID: 16967960
Bockelée-Morvan, D., Lis, D. C., Wink, J. E., et al. 2000, A&A, 353, 1101
Bocquet, R., Demaison, J., Cosléou, J., et al. 1999, J. Mol. Spectrosc., 195, 345
Bocquet, R., Demaison, J., Poteau, L., et al. 1996, J. Mol. Spectrosc., 177, 154
Bøgelund, E. G., Barr, A. G., Taquet, V., et al. 2019, A&A, 628, A2
Botta, O. & Bada, J. L. 2002, Surv. Geophys., 23, 411
Bouchez, A., Walters, A., Müller, H. S. P., et al. 2012, J. Quant. Spectr. Rad. Transf., 113, 1148
Boussessi, R., Senent, M. L., & Jaïdane, N. 2016, J. Chem. Phys., 144, 164110
Brown, R. D., Godfrey, P. D., McNaughton, D., Pierlot, A. P., & Taylor, W. H. 1990, J. Mol. Spectrosc., 140, 340
Brünken, S., Müller, H. S. P., Lewen, F., & Winnewisser, G. 2003, PCCP, 5
Burke, D. J., Puletti, F., Brown, W. A., et al. 2015, MNRAS, 447, 1444
Butcher, S. S. & Bright Wilson, Jr., E. 1964, J. Chem. Phys., 40, 1671
Butler, R. A. H., De Lucia, F. C., Petkie, D. T., et al. 2001, ApJS, 134, 319
Calcutt, H., Fiechter, M. R., Willis, E. R., et al. 2018a, A&A, 617, A95
Calcutt, H., Jørgensen, J. K., Müller, H. S. P., et al. 2018b, A&A, 616, A90
Calcutt, H., Viti, S., Codella, C., et al. 2014, MNRAS, 443, 3157
Carroll, P. B., Drouin, B. J., & Widicus Weaver, S. L. 2010, ApJ, 723, 845
Carroll, P. B., McGuire, B. A., Blake, G. A., et al. 2015, ApJ, 799, 15
Carvajal, M., Kleiner, I., & Demaison, J. 2010, ApJS, 190, 315
Caux, E., Kahane, C., Castets, A., et al. 2011, A&A, 532, A23
Cazaux, S., Tielens, A. G. G. M., Ceccarelli, C., et al. 2003, ApJ, 593, L51
Ceccarelli, C., Caselli, P., Fontani, F., et al. 2017, ApJ, 850, 176
Christen, D., Coudert, L. H., Larsson, J. A., & Cremer, D. 2001, J. Mol. Spectrosc., 205, 185
Christen, D., Coudert, L. H., Suenram, R. D., & Lovas, F. J. 1995, J. Mol. Spectrosc., 172, 57
Christen, D. & Müller, H. S. P. 2003, PCCP, 5
Chuang, K.-J., Fedoseev, G., Ioppolo, S., van Dishoeck, E. F., & Linnartz, H. 2016, MNRAS, 455, 1702
Chuang, K.-J., Fedoseev, G., Qasim, D., et al. 2018, ApJ, 853, 102
Cornet, R. A. & Winnewisser, G. 1980, J. Mol. Spectrosc., 80, 438
Coudert, L. H., Margulès, L., Vastel, C., et al. 2019, A&A, 624, A70
Coutens, A., Jørgensen, J. K., van der Wiel, M. H. D., et al. 2016, A&A, 590, 1
Coutens, A., Ligterink, N. F. W., Loison, J. C., et al. 2019, A&A, 623, L13
Coutens, A., Viti, S., Rawlings, J. M. C., et al. 2018, MNRAS, 475, 2016
Creswell, R. A. & Schwendeman, R. H. 1974, Chem. Phys. Lett., 27, 521
Crovisier, J., Bockelée-Morvan, D., Biver, N., et al. 2004, A&A, 418, L35
Cunningham, Jr., G. L., Boyd, A. W., Myers, R. J., Gwinn, W. D., & Le van, W. I. 1951, J. Chem. Phys., 19, 676
Dangoisse, D., Willemot, E., & Bellet, J. 1978, J. Mol. Spectrosc., 71, 414
Demaison, J., Dubrulle, A., Boucher, D., Burie, J., & van Eijck, B. P. 1982, J. Mol. Spectrosc., 94, 211
Demaison, J., Maes, H., Van Eijck, B. P., Wlodarczak, G., & Lasne, M. C. 1987, J. Mol. Spectrosc., 125, 214
Drozdovskaya, M. N., van Dishoeck, E. F., Jørgensen, J. K., et al. 2018, MNRAS, 476, 4949
Drozdovskaya, M. N., van Dishoeck, E. F., Rubin, M., Jørgensen, J. K., & Altwegg, K. 2019, MNRAS, 490, 50
Drozdovskaya, M. N., Walsh, C., van Dishoeck, E. F., et al. 2016, MNRAS, 462, 977
Durig, J. R., Compton, D. A. C., & McArver, A. Q. 1980, J. Chem. Phys., 73, 719
Durig, J. R., Deeb, H., Darkhalil, I. D., et al. 2011, J. Mol. Struct., 985, 202
Durig, J. R. & Larsen, R. A. 1990, J. Mol. Struct., 238, 195
Dzib, S. A., Ortiz-León, G. N., Hernández-Gómez, A., et al. 2018, A&A, 614, A20
Ehrenfreund, P., Glavin, D. P., Botta, O., Cooper, G., & Bada, J. L. 2001, Proceedings of the National Academy of Science, 98, 2138
Elkeurti, M., Coudert, L. H., Medvedev, I. R., et al. 2010, J. Mol. Spectrosc., 263, 145
Endres, C. P., Drouin, B. J., Pearson, J. C., et al. 2009, A&A, 504, 635
Endres, C. P., Schlemmer, S., Schilke, P., Stutzki, J., & Müller, H. S. P. 2016, J. Mol. Spectrosc., 327, 95
Fabricant, B., Krieger, D., & Muenter, J. S. 1977, J. Chem. Phys., 67, 1576
Favre, C., Carvajal, M., Field, D., et al. 2014, ApJS, 215, 25
Favre, C., Fedele, D., Semenov, D., et al. 2018, ApJ, 862, L2
Fayolle, E. C., Öberg, K. I., Garrod, R. T., van Dishoeck, E. F., & Bisschop, S. E. 2015, A&A, 576, A45
Fayolle, E. C., Öberg, K. I., Jørgensen, J. K., et al. 2017, Nature Astronomy, 1, 703
Fedoseev, G., Chuang, K. J., Ioppolo, S., et al. 2017, ApJ, 842, 52
Fedoseev, G., Cuppen, H. M., Ioppolo, S., Lamberts, T., & Linnartz, H. 2015a, MNRAS, 448, 1288
Fedoseev, G., Ioppolo, S., Zhao, D., Lamberts, T., & Linnartz, H. 2015b, MNRAS, 446, 439
Fisher, J., Paciga, G., Xu, L.-H., et al. 2007, J. Mol. Spectrosc., 245, 7
Fuchs, G. W., Cuppen, H. M., Ioppolo, S., et al. 2009, A&A, 505, 629
Fuchs, G. W., Fuchs, U., Giesen, T. F., & Wyrowski, F. 2005, A&A, 444, 521
Fuchs, U., Winnewisser, G., Groner, P., De Lucia, F. C., & Herbst, E. 2003, ApJS, 144, 277
Gardner, F. F., Godfrey, P. D., & Williams, D. R. 1980, MNRAS, 193, 713
Garrod, R. T. 2013, ApJ, 765, 60
Garrod, R. T. & Herbst, E. 2006, A&A, 457, 927
Garrod, R. T., Widicus Weaver, S. L., & Herbst, E. 2008, ApJ, 682, 283
Girart, J. M., Estalella, R., Palau, A., Torrelles, J. M., & Rao, R. 2014, ApJ, 780, L11
Groner, P., Albert, S., Herbst, E., & De Lucia, F. C. 1998, ApJ, 500, 1059
Groner, P., Albert, S., Herbst, E., et al. 2002, ApJS, 142, 145
Groner, P., Herbst, E., De Lucia, F. C., Drouin, B. J., & Mäder, H. 2006, Journal of Molecular Structure, 795, 173

Guarnieri, A. 2005, Zeitschrift Naturforschung Teil A, 60, 619
Guarnieri, A. & Huckaufa, A. 2003, Zeitschrift Naturforschung Teil A, 58, 275
Hardy, J. A., Cox, A. P., Fliege, E., & Dreizler, H. 1982, Zeitschrift Naturforschung Teil A, 37, 1035
Hayashi, M. & Adachi, M. 1982, J. Mol. Struct., 78, 53
Hayashi, M. & Kuwada, K. 1975, J. Mol. Struct., 28, 147
Hays, B. M. & Widicus Weaver, S. L. 2013, The Journal of Physical Chemistry A, 117, 7142, pMID: 23646865
Herbst, E. & van Dishoeck, E. F. 2009, ARA&A, 47, 427
Hirose, C. 1974, ApJ, 189, L145
Hirota, E., Sugisaki, R., Nielsen, C. J., & Sørensen, G. O. 1974, J. Mol. Spectrosc., 49, 251
Hocking, W. H., Gerry, M. C. L., & Winnewisser, G. 1975, Can. J. Phys., 53, 1869
Hollis, J. M., Vogel, S. N., Snyder, L. E., Jewell, P. R., & Lovas, F. J. 2001, ApJ, 554, L81
Hunter, J. D. 2007, Comput. Sci. Eng., 9, 90
Ikeda, M., Duan, Y.-B., Tsunekawa, S., & Takagi, K. 1998, ApJS, 117, 249
Ilyushin, V., Kleiner, I., & Lovas, F. J. 2008, J. Phys. Chem. Ref. Data, 37, 97
Ilyushin, V. V., Alekseev, E. A., Dyubko, S. F., & Kleiner, I. 2003, J. Mol. Spectrosc., 220, 170
Ilyushin, V. V., Alekseev, E. A., Dyubko, S. F., et al. 2001, J. Mol. Spectrosc., 205, 286
Ilyushin, V. V., Endres, C. P., Lewen, F., Schlemmer, S., & Drouin, B. J. 2013, J. Mol. Spectrosc., 290, 31
Jacobsen, S. K., Jørgensen, J. K., van der Wiel, M. H. D., et al. 2018, A&A, 612, A72
Johns, J. W. C. & McKellar, A. R. W. 1977, J. Mol. Spectrosc., 64, 327
Johns, J. W. C., Nemes, L., Yamada, K. M. T., et al. 1992, J. Mol. Spectrosc., 156, 501
Johnson, H. R. & Strandberg, M. W. P. 1952, J. Chem. Phys., 20, 687
Jones, E., Oliphant, T., Peterson, P., et al. 2001, SciPy: Open source scientific tools for Python, [Online; accessed <today>]
Jørgensen, J. K., Bourke, T. L., Nguyen Luong, Q., & Takakuwa, S. 2011, A&A, 534, A100
Jørgensen, J. K., Favre, C., Bisschop, S. E., et al. 2012, ApJ, 757, L4
Jørgensen, J. K., Müller, H. S. P., Calcutt, H., et al. 2018, A&A, 620, A170
Jørgensen, J. K., van der Wiel, M. H. D., Coutens, A., et al. 2016, A&A, 595, A117
Kleiner, I., Lovas, F. J., & Godefroid, M. 1996, J. Phys. Chem. Ref. Data, 25, 1113
Kobayashi, K., Sakai, Y., Tsunekawa, S., et al. 2016, J. Mol. Spectrosc., 321, 63
Koerber, M., Bisschop, S. E., Endres, C. P., et al. 2013, A&A, 558, A112
Krisher, L. C. & Saegebarth, E. 1971, J. Chem. Phys., 54, 4553
Kryvda, A. V., Gerasimov, V. G., Dyubko, S. F., Alekseev, E. A., & Motiyenko, R. A. 2009, J. Mol. Spectrosc., 254, 28
Kukolich, S. G. & Nelson, A. C. 1971, Chem. Phys. Lett., 11, 383
Kurland, R. J. & Bright Wilson, Jr., E. 1957, J. Chem. Phys., 27, 585
Kuze, H., Kuga, T., & Shimizu, T. 1982, J. Mol. Spectrosc., 93, 248
Lapinov, A. V., Golubiatnikov, G. Y., Markov, V. N., & Guarnieri, A. 2007, AstL, 33, 121
Lattanzi, V., Walters, A., Drouin, B. J., & Pearson, J. C. 2008, ApJS, 176, 536
Le Roy, L., Altwegg, K., Balsiger, H., et al. 2015, A&A, 583, A1
Lerner, R. G., Dailey, B. P., & Friend, J. P. 1957, J. Chem. Phys., 26, 680
Li, J., Shen, Z., Wang, J., et al. 2017, ApJ, 849, 115
Ligterink, N. F. W., Coutens, A., Kofman, V., et al. 2017, MNRAS, 469, 2219
Lohilahti, J. & Horneman, V.-M. 2004, J. Mol. Spectrosc., 228, 1
López-Sepulcre, A., Sakai, N., Neri, R., et al. 2017, A&A, 606, A121
Lykke, J. M., Coutens, A., Jørgensen, J. K., et al. 2017, A&A, 597, A53
Maeda, A., De Lucia, F. C., & Herbst, E. 2008a, J. Mol. Spectrosc., 251, 293
Maeda, A., Medvedev, I. R., De Lucia, F. C., Herbst, E., & Groner, P. 2008b, ApJS, 175, 138
Manigand, S., Calcutt, H., Jørgensen, J. K., et al. 2018, A&A, subm.
Marstokk, K.-M. & Møllendal, H. 1970, J. Mol. Struct., 5, 205
Marstokk, K.-M. & Møllendal, H. 1973, J. Mol. Struct., 16, 259
Martinache, L. & Bauder, A. 1989, Chem. Phys. Lett., 164, 657
McGuire, B. A., Shingledecker, C. N., Willis, E. R., et al. 2017, ApJ, 851, L46
McMullin, J. P., Waters, B., Schiebel, D., Young, W., & Golap, K. 2007, in Astronomical Society of the Pacific Conference Series, Vol. 376, Astronomical Data Analysis Software and Systems XVI, ed. R. A. Shaw, F. Hill, & D. J. Bell, 127
Medcraft, C., Thompson, C. D., Robertson, E. G., Appadoo, D. R. T., & McNaughton, D. 2012, ApJ, 753, 18
Milam, S. N., Savage, C., Brewster, M. A., Ziurys, L. M., & Wyckoff, S. 2005, ApJ, 634, 1126
Mollabashi, M., Lees, R. M., Xu, L.-H., & Bakota, M. 1993, Int. J. Infrared Millimeter Waves, 14, 2569
Morina, L., Obst, S., Unrath, M., et al. 2019, Journal of Molecular Spectroscopy, 356, 1
Moskienko, E. M. & Dyubko, S. F. 1991, Radiophys. Quantum Electron., 34, 181
Motiyenko, R. A., Margulès, L., Despois, D., & Guillemin, J.-C. 2018, PCCP, 20, 5509
Motiyenko, R. A., Tercero, B., Cernicharo, J., & Margulès, L. 2012, A&A, 548, A71
Mukhopadhyay, I. 2016, nfrared Phys. Technol., 75, 139
Müller, H. S. P., Belloche, A., Xu, L.-H., et al. 2016, A&A, 587, A92
Müller, H. S. P. & Christen, D. 2004, J. Mol. Spectrosc., 228, 298
Müller, H. S. P., Gendriesch, R., Lewen, F., & Winnewisser, G. 2000a, Zeitschrift Naturforschung Teil A, 55
Müller, H. S. P., Gendriesch, R., Margulès, L., et al. 2000b, PCCP, 2
Müller, H. S. P. & Lewen, F. 2017, J. Mol. Spectrosc., 331, 28
Müller, H. S. P., Schlöder, F., Stutzki, J., & Winnewisser, G. 2005, J. Mol. Struct., 742, 215
Müller, H. S. P., Thorwirth, S., Roth, D. A., & Winnewisser, G. 2001, A&A, 370, L49
Müller, H. S. P., Winnewisser, G., Demaison, J., Perrin, A., & Valentin, A. 2000c, J. Mol. Spectrosc., 200, 143
Müller, H. S. P., Xu, L.-H., & van der Tak, F. 2006, J. Mol. Struct., 795, 114
Ndao, M., Kwabia Tchana, F., Coudert, L. H., et al. 2016, J. Mol. Spectrosc., 326, 136
Niedenhoff, M., Yamada, K. M. T., Belov, S. P., & Winnewisser, G. 1995, J. Mol. Spectrosc., 174, 151
Nielsen, C. J. 1973, PhD thesis, Københavns Universitet, Denmark
Öberg, K. I., Furuya, K., Loomis, R., et al. 2015, ApJ, 810, 112
Öberg, K. I., Garrod, R. T., van Dishoeck, E. F., & Linnartz, H. 2009, A&A, 504, 891
Ochsenbein, F., Bauer, P., & Marcout, J. 2000, A&AS, 143, 23
Oldag, F. & Sutter, D. H. 1992, Zeitschrift Naturforschung Teil A, 47, 527
Ordu, M. H., Zingsheim, O., Belloche, A., et al. 2019, A&A, 629, A72
Ospina-Zamudio, J., Lefloch, B., Ceccarelli, C., et al. 2018, A&A, 618, A145
Oya, Y., Sakai, N., López-Sepulcre, A., et al. 2016, ApJ, 824, 88
Paardekooper, D. M., Bossa, J. B., & Linnartz, H. 2016, A&A, 592, A67
Pan, J., Albert, S., Sastry, K. V. L. N., Herbst, E., & De Lucia, F. C. 1998, ApJ, 499, 517
Parise, B., Castets, A., Herbst, E., et al. 2004, A&A, 416, 159
Parise, B., Ceccarelli, C., Tielens, A. G. G. M., et al. 2002, A&A, 393, L49
Pearson, J. C., Brauer, C. S., & Drouin, B. J. 2008, J. Mol. Spectrosc., 251, 394
Pearson, J. C., Sastry, K. V. L. N., Herbst, E., & De Lucia, F. C. 1996, J. Mol. Spectrosc., 175, 246
Pearson, J. C., Sastry, K. V. L. N., Winnewisser, M., Herbst, E., & De Lucia, F. C. 1995, J. Phys. Chem. Ref. Data, 24, 1
Pearson, J. C., Yu, S., & Drouin, B. J. 2012, J. Mol. Spectrosc., 280, 119
Penzias, A. A. 1981, ApJ, 249, 518
Persson, M. V., Jørgensen, J. K., Müller, H. S. P., et al. 2018, A&A, 610, A54
Persson, M. V., Jørgensen, J. K., & van Dishoeck, E. F. 2012, A&A, 541, A39
Peter, R. & Dreizler, H. 1965, Zeitschrift Naturforschung Teil A, 20, 301
Pickett, H. M., Poynter, R. L., Cohen, E. A., et al. 1998, J. Quant. Spectr. Rad. Transf., 60, 883
Pineda, J. E., Maury, A. J., Fuller, G. A., et al. 2012, A&A, 544, L7
Potin, S., Manigand, S., Beck, P., Wolters, C., & Schmitt, B. 2019, subm., Icarus
Qasim, D., Fedoseev, G., Chuang, K. J., et al. 2019a, A&A, 627, A1
Qasim, D., Lamberts, T., He, J., et al. 2019b, A&A, 626, A118
Richard, C., Margulès, L., Caux, E., et al. 2013, A&A, 552, A117
Robitaille, T. P., Tollerud, E. J., Greenfield, P., et al. 2013, A&A, 558, A33
Senent, M., Ruiz, R., Villa, M., & Domínguez-Gómez, R. 2009, J. Chem. Phys., 130, 064101
Skouteris, D., Balucani, N., Ceccarelli, C., et al. 2019, MNRAS, 482, 3567
Skouteris, D., Balucani, N., Ceccarelli, C., et al. 2018, ApJ, 854, 135
Skouteris, D., Vazart, F., Ceccarelli, C., et al. 2017, MNRAS, 468, L1
Sutter, D. H. & Dreizler, H. 2000, Zeitschrift Naturforschung Teil A, 55, 695
Tabor, W. J. 1957, J. Chem. Phys., 27, 974
Taquet, V., Wirström, E. S., Charnley, S. B., et al. 2017, A&A, 607, A20
Tercero, B., Cernicharo, J., López, A., et al. 2015, A&A, 582, L1
Tercero, B., Cuadrado, S., López, A., et al. 2018, A&A, 620, L6
Tsunekawa, S., Kinai, Y., Kondo, Y., et al. 2011, Toyama Univ. Mol. Spectrosc. Data, vol. 4
Tsunekawa, S., Kinai, Y., Kondo, Y., Odashima, H., & Takagi, K. 2003, Molecules, 8, 103
Turner, P. H. & Cox, A. P. 1976, Chem. Phys. Lett., 42, 84
Turner, P. H., Cox, A. P., & Hardy, J. A. 1981, J. Chem. Soc., Faraday Trans. 2, 77, 1217
Vacherand, J. M., Van Eijck, B. P., Burie, J., & Demaison, J. 1986, J. Mol. Spectrosc., 118, 355
van der Walt, S., Colbert, S. C., & Varoquaux, G. 2011, Computing in Science Engineering, 13, 22
van der Wiel, M. H. D., Jacobsen, S. K., Jørgensen, J. K., et al. 2019, arXiv e-prints, arXiv:1903.12606

van Dishoeck, E. F., Blake, G. A., Jansen, D. J., & Groesbeck, T. D. 1995, ApJ, 447, 760
van Eijck, B. P. & van Duijneveldt, F. B. 1983, J. Mol. Spectrosc., 102, 273
van Eijck, B. P., van Opheusden, J., van Schaik, M. M. M., & van Zoeren, E. 1981, J. Mol. Spectrosc., 86, 465
Vorob'eva, E. M. & Dyubko, S. F. 1994, Radiophys. Quantum Electron., 37, 155
Walsh, C., Juhász, A., Meeus, G., et al. 2016, ApJ, 831, 200
Walsh, M. S., Xu, L.-H., & Lees, R. M. 1998, J. Mol. Spectrosc., 188, 85
Walters, A., Schäfer, M., Ordu, M. H., et al. 2015, J. Mol. Spectrosc., 314, 6
Wellington Davis, R., Robiette, A. G., Gerry, M. C. L., Bjarnov, E., & Winnemisser, G. 1980, J. Mol. Spectrosc., 81, 93
Widicus Weaver, S. L., Butler, R. A. H., Drouin, B. J., et al. 2005, ApJS, 158, 188
Willaert, F., Møllendal, H., Alekseev, E., et al. 2006, J. Mol. Struct., 795, 4
Willemot, E., Dangoisse, D., Monnanteuil, N., & Bellet, J. 1980, J. Phys. Chem. Ref. Data, 9, 59
Wilson, T. L. 1999, Reports on Progress in Physics, 62, 143
Winnewisser, M., Winnewisser, B. P., Stein, M., et al. 2002, J. Mol. Spectrosc., 216, 259
Wlodarczak, G. & Demaison, J. 1988, A&A, 192, 313
Xu, L.-H. & Lovas, F. J. 1997, J. Phys. Chem. Ref. Data, 26, 17
Xu, L. H., Müller, H. S. P., van der Tak, F. F. S., & Thorwirth, S. 2004, J. Mol. Spectrosc., 228, 220
Xu, L.-H., Walsh, M. S., & Lees, R. M. 1996, J. Mol. Spectrosc., 179, 269
Xue, C., Remijan, A. J., Burkhardt, A. M., & Herbst, E. 2019, ApJ, 871, 112
Zakharenko, O., Motiyenko, R. A., Margulès, L., & Huet, T. R. 2015, J. Mol. Spectrosc., 317, 41
Zingsheim, O., Müller, H. S. P., Lewen, F., Jørgensen, J. K., & Schlemmer, S. 2017, J. Mol. Spectrosc., 342, 125

Appendix A: Statistical distance

The statistical distance of the abundance of a species X relative to a species Y between IRAS 16293A and IRAS 16293B is calculated as follows:

$$S_{X/Y} = \frac{\left(\frac{N_X}{N_Y}\right)_{\rm A} - \left(\frac{N_X}{N_Y}\right)_{\rm B}}{\sqrt{\sigma_{\rm A}^2 + \sigma_{\rm B}^2}} \tag{A.1}$$

in which $\sigma_{\rm A}$ and $\sigma_{\rm B}$ are the uncertainties of the column density ratios $\left(\frac{N_X}{N_Y}\right)_{\rm A}$ and $\left(\frac{N_X}{N_Y}\right)_{\rm B}$, respectively. The value of $S_{X/Y}$ corresponds to the significance of the distance in terms of the number of σ.

Appendix B: Monte-Carlo error estimation

Because of the non-linearity of the model used in this study and the non-standard χ^2 minimisation method, the uncertainties on the excitation temperature and the column density are not derivable from the covariance matrix, usually calculated with the χ^2 minimisation methods. In this case, the Monte Carlo (MC) simulation becomes a convenient tool to estimate the uncertainties from the posterior probability distributions of each parameter of the model. In this section, we describe the bootstrap algorithm, which is a specific class of Monte Carlo simulations, that was tested to estimate the uncertainties of the parameters of the model.

Consider the data fitted as a vector $\boldsymbol{S}$ of N elements, which are the data points:

$$\boldsymbol{S} = (s_0,\ s_1,\ s_2, \cdots). \tag{B.1}$$

A Gaussian noise $\boldsymbol{\epsilon}$ is defined with the same logic:

$$\boldsymbol{\epsilon} = (\epsilon_0,\ \epsilon_1,\ \epsilon_2, \cdots). \tag{B.2}$$

The χ^2 minimisation can be represented by a function F_{χ^2} that transforms a data vector $\boldsymbol{S}$ into a parameter vector $\boldsymbol{P}$, which is the best fit parameters of the model for the given data. The inverse function F^{-1} is thus the fitting model, that is, the synthetic spectrum in the present study:

$$\boldsymbol{P} = \quad (p_0,\ p_1,\ p_2, \cdots) \tag{B.3}$$

$$F_{\chi^2}: \quad \boldsymbol{S} \longrightarrow F_{\chi^2}(\boldsymbol{S}) = \boldsymbol{P} \tag{B.4}$$

$$F^{-1}: \quad \boldsymbol{P} \longrightarrow F^{-1}(\boldsymbol{P}) = \tilde{\boldsymbol{S}} \tag{B.5}$$

in which $\tilde{\boldsymbol{S}}$ is the closest synthetic spectrum to the data $\boldsymbol{S}$. The MC method used in this study is a simple application of the Markov-Chain MC simulations where: the prior distribution is a group of normally distributed noise $\{\boldsymbol{\epsilon_i}\}_{N_{MC}}$ of a width equivalent to the uncertainty σ of the data, with N_{MC} the total number of walkers; the sampler is the χ^2 minimisation function F_{χ^2}; the probability for a walker to jump to a worse position in the parameter space is null; and only the final position of each walker is kept.

In this particular case, the posterior probability distributions are fully dependent on the prior distributions. From the MC simulation, we get a group of parameter vectors:

$$\mathcal{P} = \left\{F_{\chi 2}\left(\boldsymbol{S} + \boldsymbol{\epsilon_i}\right)\right\}_{N_{MC}} \tag{B.6}$$

$$= \{(p_0,\ p_1,\ p_2, \cdots)_0,\ (p_0,\ p_1,\ p_2, \cdots)_1, \cdots\}_{N_{MC}} \tag{B.7}$$

$$\mathcal{P}^T = \left(\{p_0\}_{N_{MC}},\ \{p_1\}_{N_{MC}},\ \{p_2\}_{N_{MC}}, \cdots\right) \tag{B.8}$$

$$\mathcal{P}^T = (\mathcal{P}_0,\ \mathcal{P}_1,\ \mathcal{P}_2, \cdots) \tag{B.9}$$

where $\mathcal{P}_i$ is the group of parameters p_i. The distribution of $\mathcal{P}_i$, called the posterior probability distribution of p_i, gives the needed information for the fitted parameters. It is maximal for the best fit value and the width at half-maximum of each side of the distribution corresponds to the negative and positive uncertainties on p_i.

Appendix C: Laboratory spectroscopic data

Most of the analysed species do not assume any excited vibrational or torsional level contributions to the partition function at low rotational temperatures. However, they are all detected at rotational temperatures above 100 K, where the vibrational and torsional contribution can be significant. Thus, it is necessary to detail the spectroscopic dataset used for each species. In this study, a vibrational correction factor > 1.1 is considered significant and is not applied to the column density derived from the synthetic spectrum fit if it lies below this value.

Spectroscopic data for $CH_3^{18}OH$ are provided in the Cologne Database of Molecular Spectroscopy[2] (CDMS, Endres et al. (2016) and Müller et al. (2005, 2001)) from the spectroscopic analyses of Fisher et al. (2007) and Ikeda et al. (1998). The entry of $^{13}CH_3OH$, from the CDMS catalogue, is based on Xu & Lovas (1997) and Xu et al. (1996). The dipole moment is assumed to be the same as of the main isotopomer, and the partition function takes only the permanent dipole moment into account. The spectroscopy of CH_2DOH is taken from the Jet Propulsion Laboratory catalogue[3] (JPL, Pickett et al. 1998), where the entry is based on Pearson et al. (2012). The frequency list for CHD_2OH is based on Ndao et al. (2016), with additional transitions in the range of the PILS observations from Mukhopadhyay (2016). The data do not include line strengths or the partition function; however, the frequencies are assigned with uncertainty much lower than the resolution of the observations used in this study.

The spectroscopic data for CH_3OCHO isotopologues, except for $CH_3O^{13}CHO$, are described in Manigand et al. (2018), and references therein, from which the derived column densities for source A are taken. The CDMS entry for $CH_3O^{13}CHO$ is based on Carvajal et al. (2010), with measured data in the range of the PILS survey from Willaert et al. (2006), Maeda et al. (2008b), and Maeda et al. (2008a). The vibrational contribution of $CH_3O^{13}CHO$ is already included in the CDMS entry (Favre et al. 2014).

The data for CH_3OCH_3 are provided by the CDMS catalogue. The entry is based on Endres et al. (2009) with additional data in the range of our survey from Groner et al. (1998). The mono-deuterated dimethyl ether (CH_2DOCH_3) exists in two forms, symmetric and asymmetric. The data of both conformers are taken from Richard et al. (2013). The data of $CH_3O^{13}CH_3$ are taken from Koerber et al. (2013) and from the Vizier Online Data Catalogue, which is from the Centre de Données Astronomiques de Strasbourg[4] (CDS). The contribution from excited vibrational levels is estimated to be 1.15 at T_{ex} = 100 K for the ^{13}C and deuterated isotopologues.

Spectroscopic data for CH_3CHO can be found in the JPL catalogue. The entry is based on Kleiner et al. (1996), with experimental transition frequencies in the range of our survey from Belov et al. (1993). The CDMS entry for CH_3CDO is based on Coudert et al. (2019). The fit and the experimental frequencies used are described in Elkeurti et al. (2010), with additional

[2] https://www.astro.uni-koeln.de/cdms
[3] https://spec.jpl.nasa.gov/
[4] http://cdsarc.u-strasbg.fr/

data below 50 GHz taken from Martinache & Bauder (1989). The partition function includes the first three excited torsional mode contributions and is reliable at 140 K. The spectroscopy of the other deuterated isotopologue CH_2DCHO is also described in Coudert et al. (2019) with additional data taken from Turner & Cox (1976) and Turner et al. (1981). The contribution of the lowest torsional mode and the small amplitude vibration are included in the partition function. The partition function converged up to about 100 K. Therefore, vibrational corrections are neglected at 140 K.

C_2H_5OH isotopologues exist under two isomeric forms, anti and gauche, depending on the OH group torsion. In addition, the gauche conformer has two degenerated states. The extended analysis of the vibrational ground state is provided by Pearson et al. (2008). However, Müller et al. (2016) find that the predicted intensities do not fit the Sgr B2(N2) emission at 3 mm, and they provide a corrected entry in the CDMS catalogue. This entry combines the anti and the gauche conformer transitions and includes data from Pearson et al. (1995, 1996) in the range of the PILS survey. ^{13}C and deuterated C_2H_5OH isotopologues spectroscopic data are taken from corresponding CDMS entries, based on Bouchez et al. (2012) and Walters et al. (2015), respectively. However, these data consider only the anti conformer. The column density has to be multiplied by a factor of ∼2.32 at T_{ex} = 135 K to take the gauche conformer into account (Müller et al. 2016; Jørgensen et al. 2018). The contribution from excited vibrational levels is dominated by the two torsional modes of the methyl group (Durig & Larsen 1990)[5]. The vibrational correction factor is 1.24 for the main isotopologue (Durig et al. 2011) and is applicable for the ^{13}C and deuterated isotopologues.

Spectroscopic data of the H_2CO isotopologues are taken from the corresponding CDMS entries and are the result of several contributions over the past four decades. H_2CO, $H_2C^{18}O$ and $H_2C^{17}O$ entries are based on Müller & Lewen (2017), the $H_2^{13}CO$ entry is based on Müller et al. (2000b), and HDCO and D_2CO entries are based on Zakharenko et al. (2015). Additional data were taken from Brünken et al. (2003), Bocquet et al. (1996) and Cornet & Winnewisser (1980) for H_2CO as well as a few transition frequencies of $H_2C^{18}O$ and $H_2^{13}CO$. Müller et al. (2000c) provided the ground state combination differences employed in the spectroscopic analysis of H_2CO. For the two deuterated isotopologues HDCO and D_2CO, the data were taken from Lohilahti & Horneman (2004), Bocquet et al. (1999) and Dangoisse et al. (1978). Additional $H_2C^{18}O$ transition frequencies were taken from Müller et al. (2000a). The dipole moments were measured by Fabricant et al. (1977) and Johns & McKellar (1977). The dipole moments of $H_2C^{17}O$ and $H_2C^{18}O$ are assumed to be the same as the H_2CO one. The vibration state energies are way too high to significantly affect the partition function at 155 K.

The publicly available JPL entry for CH_3COCH_3, also called propanone, is based on Groner et al. (2002), with the rotational partitioning and the line strength calculation. This study used additional data from Oldag & Sutter (1992), Vacherand et al. (1986) and Peter & Dreizler (1965) for transition frequencies up to 300 GHz. In the present study, we used an updated version of the spectroscopic data, which will be available on CDMS. This entry is based on the study of Ordu et al. (2019), which includes the previous linelists as well as those from the first two torsional excited states taken from Morina et al. (2019) and Groner et al. (2006). The contribution from excited vibrational level ν=1 is taken into account in the harmonic approximation and thus in the partition function.

c-H_2COCH_2 data are provided by the CDMS catalogue. The entry was based on experimental data taken from Hirose (1974), Creswell & Schwendeman (1974) and Pan et al. (1998). Much more additional data from Medcraft et al. (2012) enriched the set, extending the frequency range from 358 GHz to 4 THz. The dipole moment is taken from Cunningham et al. (1951). The vibrational correction factor is insignificant at 95 K.

The rotational spectrum of CH_3COOH was first extensively analysed by Ilyushin et al. (2008), which was based on a fair amount of measured spectroscopic data from 8 to 358 GHz taken from Tabor (1957), Krisher & Saegebarth (1971), van Eijck et al. (1981), van Eijck & van Duijneveldt (1983), Demaison et al. (1982), Wlodarczak & Demaison (1988), Ilyushin et al. (2001) and Ilyushin et al. (2003). The present study uses the recent datafile provided by Ilyushin et al. (2013). This last study considerably extended the number of measured transition frequencies up to 845 GHz and observed the first two torsional excited states. The partition function takes into account these states and more excited torsional up to v_t = 8 in the vibrational ground state. The low vibration states are too energetically high to make the vibrational correction factor significant at 110 K.

The JPL catalogue provides the line list for $CH_2(OH)CHO$. The entry is based on the rotational lines collection of Carroll et al. (2010). Previous laboratory measurements were carried out by Marstokk & Møllendal (1970), Marstokk & Møllendal (1973) and Butler et al. (2001) and served as the base for the latest study. The partition function was previously calculated by Widicus Weaver et al. (2005) over a measured frequency range from 72 to 122.5 GHz and included the ground state and three partially populated vibrational states at room temperature. Carroll et al. (2010) find a systematic bias in the lines with $K_a \sim 28-31$ and they corrected iteratively the assignment in the JPL line list.

NH_2CHO data used in this study are provided by the CDMS catalogue. The dipole moment was measured by Kurland & Bright Wilson (1957). The observed experimental frequencies are taken from Kukolich & Nelson (1971), Nielsen (1973), Hirota et al. (1974), Gardner et al. (1980), Moskienko & Dyubko (1991), Vorob'eva & Dyubko (1994), Blanco et al. (2006) and Kryvda et al. (2009). The latest study (Motiyenko et al. 2012) considerably extended the frequency range of measured transitions up to 930 GHz. The partition function does not include any contributions from the excited vibrational state. However, the lowest vibration state energy of 288 cm^{-1} leads to the highest vibration correction factor, which is lower than 1.1 at 145 K.

Spectroscopic data of the HCOOH isotopologues are provided in the CDMS catalogue for *t*-HCOOH and by JPL for *t*-$H^{13}COOH$, *t*-DCOOH, and *t*-HCOOD. The CDMS entry for the main isotopologue is based on Winnewisser et al. (2002) with additional data from previous studies (Auwera 1992; Willemot et al. 1980). The JPL entries are based on the same study of Lattanzi et al. (2008) gathering the analysis of these three isotopologues. Experimental measurements were taken from Bellet et al. (1971) and Lerner et al. (1957) for the three entries, and Wellington Davis et al. (1980), Winnewisser et al. (2002) only for the *t*-$H^{13}COOH$ entry. The dipole moment is assumed to be the same as the main isotopologue, which was measured by Kuze et al. (1982). The excited vibrational state, especially ν_7 and ν_9, was also measured for the ^{13}C and deuterated isotopologues in the studies of Baskakov et al. (2006), Baskakov et al. (1999) and Baskakov (1996). Vibration correction factors are neglected at 90 K for both the main and deuterated species.

[5] It is the combination of four torsional transitions at 244.4 and 231.1 cm^{-1} of the trans conformer and 490.0 and 453.0 cm^{-1} of the gauche conformer.

The CDMS entries for CH_2CO isotopologues are based on Guarnieri & Huckaufa (2003) and on Guarnieri (2005) for the deuterated isotopologues (CHDCO). Laboratory measurements of the different isotopologues are taken from Johnson & Strandberg (1952), Brown et al. (1990), Johns et al. (1992) and Sutter & Dreizler (2000). The dipole moments were calculated by Fabricant et al. (1977). Vibrations contributions are negligible at 135 K for both isotopologues.

$(CH_2OH)_2$ has three coupled rotors along the molecular chain. It can exist in a total of ten stable configurations (Christen et al. 2001) based on the orientation of the two OH groups at both ends of the carbon chain. Most of the transitions, especially the low-energy rotational transitions, are emitted from the two lowest fundamental state conformers *aGg'*-$(CH_2OH)_2$ and *gGg'*-$(CH_2OH)_2$, the second one lying 290 K above *aGg'* (Müller & Christen 2004). The spectroscopic data used here are taken from the CDMS entries. Experimental measurements and extensive analysis were carried out by Christen et al. (1995) and Christen & Müller (2003) for *aGg'* and by Christen et al. (2001) and Müller & Christen (2004) for gGg', up to 370 and 579 GHz, respectively. Concerning the gGg' conformer, the line strength and partition function were treated as if the conformer was the lowest conformer energy. The ground state energy of 290 K contributes to the line strengths by a factor of 2.35 at 145 K (Müller & Christen 2004). The vibrational correction factor at 145 K of 1.75, which includes the interactions between *gGg'* and *aGg'*, were calculated in the anharmonic approximation from Boussessi et al. (2016) for both conformers.

t-$C_2H_5OCH_3$ data were taken from a preliminary CDMS entry. They are based on Fuchs et al. (2003), with significant additional data from Kobayashi et al. (2016) as well as the experimental measurements from Hayashi & Adachi (1982), Tsunekawa et al. (2003), and Tsunekawa et al. (2011). The dipole moment was measured by Hayashi & Kuwada (1975). Torsional and vibrational transitions were studied by Senent et al. (2009), providing a future basis for determining the contribution of higher vibrational state energies to the partition function. The partition function and the line strength were revised by H. S. P. Müller. With the lowest vibrations at 288 cm^{-1}, the vibrational correction factor is negligible.

Regarding HNCO isotopologues, the spectroscopic data are taken from the CDMS entry for HNCO, and from the JPL entry for DNCO. The CDMS entry is based on the work of Lapinov et al. (2007), using additional data from Kukolich & Nelson (1971), Hocking et al. (1975) and Niedenhoff et al. (1995). The JPL entry was last updated in 1987 and only includes the frequencies from Hocking et al. (1975). However, the frequency uncertainties are lower than 0.4 MHz in the range of the PILS observations, except for the transitions at 346.027, 346.176, 346.380, and 346.541 GHz. These transitions correspond to very high upper state energies (i.e. > 1000 K) and they are not populated in the temperature and density ranges of IRAS 16293; therefore, the spectroscopy is reliable. We note that the HNCO partition function does not take into account the spin multiplicity of the ^{14}N nucleus. Vibration correction factors are negligible at 180 K due to the high lowest vibration contributions of 577 and ~460 cm^{-1} for HNCO and DNCO, respectively.

CH_3OCH_2OH spectroscopy has been investigated very recently because of its lower dipole moment, which makes this species more difficult to detect in space. The data used are based on the work of Motiyenko et al. (2018). They acquired the first measurements of rotation transitions between 150 and 460 GHz. The line strength and the partition function have not been published yet; however, they have been kindly provided by B. McGuire under the approval of R. A. Motiyenko. Based on the calculated vibrations (harmonic) from Hays & Widicus Weaver (2013), the vibrational correction factor is 1.55 at 130 K.

The spectroscopic data of C_2H_5CHO were found on the CDMS database. The CDMS entry is largely based on the recent study of Zingsheim et al. (2017) with additional data taken from Hardy et al. (1982) and Demaison et al. (1987), though they were remeasured in the most recent study. The dipole moment was measured by Butcher & Bright Wilson (1964). The partition function takes into account the ground vibrational state alone. The vibration correction factor is 1.42 at 120 K (Durig et al. 1980).

Appendix D: Identification of CHD_2OH transitions

The identified lines of CHD_2OH are given in this section, in Table D.1. The unblended lines alone were fitted using a Gaussian line profile and plotted in Figures D.1 and D.2.

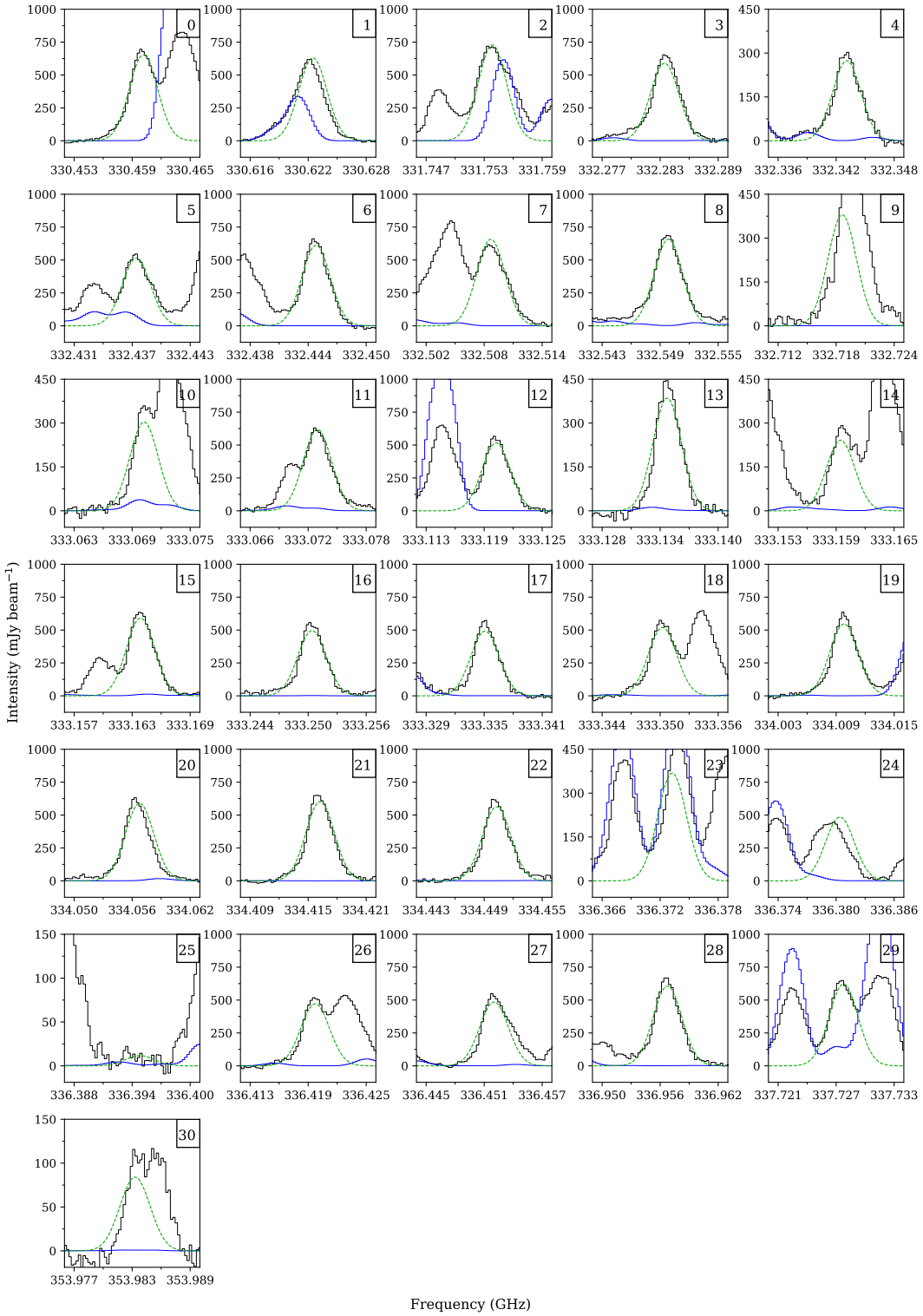


Fig. D.1: Selection of CHD_2OH identified lines in the data (in black) with the Gaussian fit in green dashed line, with fixed central velocity and FWHM. The same reference spectrum used in the analysis is represented in blue. The squared number in the top-right corner corresponds to the identification number of the transition, i.e. the panel number in Table D.1.

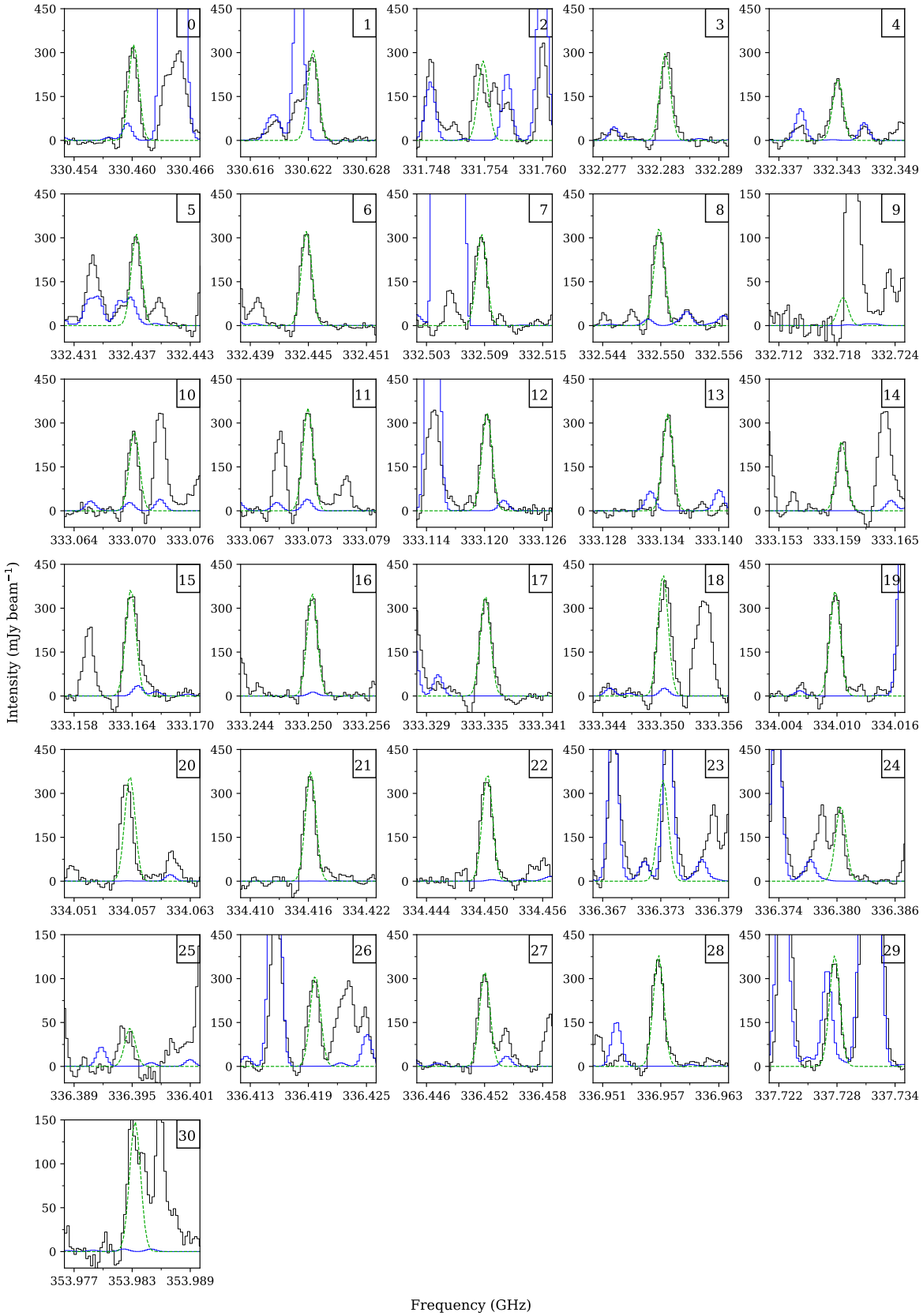


Fig. D.2: Selection of CHD_2OH identified lines in the data (in black) with the Gaussian fit in green dashed line, with fixed central velocity and FWHM. The same reference spectrum used in the analysis is represented in blue. The squared number in the top-right corner corresponds to the identification number of the transition, i.e. the panel number in Table D.1.

Table D.1: List of the CHD_2OH identified lines. The quantum numbers are taken from Mukhopadhyay (2016).

Transition (J", K") → (J', K')[a]	Frequency (GHz)	panel number[b]	$W_{\rm IRAS\ 16293A}$ (Jy beam^{-1} km s^{-1})	$W_{\rm IRAS\ 16293B}$ (Jy beam^{-1} km s^{-1})
(7, 1 + e_1) → (8, 1 + e_1)	330.4602	0	–	0.362 ± 0.013
(7, 0o_1+) → (8, 0o_1+)	330.6225	1	–	–
(7, 0e_0+) → (8, 0e_0+)	331.7538	2	–	–
(7, 0e_1+) → (8, 0e_1+)	332.2835	3	2.129 ± 0.078	0.314 ± 0.014
(7, 7 ± e_1) → (8, 7 ± e_1)	332.3431	4	0.938 ± 0.079	0.239 ± 0.014
(7, 6 ± e_1) → (8, 6 ± e_1)	332.4374	5	–	0.349 ± 0.013
(7, 2 − e_1) → (8, 2 − e_1)	332.4448	6	2.139 ± 0.094	0.353 ± 0.016
(7, 5 ± e_1) → (8, 5 ± e_1)	332.5087	7	–	0.353 ± 0.015
(7, 4 ± e_1) → (8, 4 ± e_1)	332.5498	8	2.382 ± 0.081	0.370 ± 0.014
(7, 2 + e_1) → (8, 2 + e_1)	332.7186	9	–	–
(7, 7e_0±) → (8, 7e_0±)	333.0702	10	–	0.286 ± 0.014
(7, 2 − o_1) → (8, 2 − o_1)	333.0730	11	–	0.391 ± 0.016
(7, 5 ± o_1) → (8, 5 ± o_1)	333.1202	12	2.290 ± 0.107	0.376 ± 0.015
(7, 6 ± o_1) → (8, 6 ± o_1)	333.1347	13	1.195 ± 0.081	0.350 ± 0.016
(7, 6e_0±) → (8, 6e_0±)	333.1595	14	–	0.254 ± 0.015
(7, 7 ± o_1) → (8, 7 ± o_1)	333.1639	15	2.403 ± 0.091	0.442 ± 0.016
(7, 5e_0±) → (8, 5e_0±)	333.2504	16	1.645 ± 0.082	0.396 ± 0.015
(7, 3 + e_1) → (8, 3 + e_1)	333.3351	17	1.579 ± 0.054	0.371 ± 0.013
(7, 3 + o_1) → (8, 3 + o_1)	333.3361	17	1.579 ± 0.054	0.371 ± 0.013
(7, 3 − o_1) → (8, 3 − o_1)	333.3502	18	–	0.467 ± 0.013
(7, 4e_0±) → (8, 4e_0±)	333.3502	18	–	0.467 ± 0.013
(7, 3 − e_1) → (8, 3 − e_1)	333.3509	18	–	0.467 ± 0.013
(7, 2 − e_0) → (8, 2 − e_0)	334.0098	19	1.904 ± 0.080	0.389 ± 0.014
(7, 2 + e_0) → (8, 2 + e_0)	334.0568	20	1.849 ± 0.074	0.362 ± 0.012
(7, 1 − e_1) → (8, 1 − e_1)	334.4162	21	1.929 ± 0.069	0.407 ± 0.013
(7, 2 + o_1) → (8, 2 + o_1)	334.4503	22	1.856 ± 0.079	0.429 ± 0.015
(4, 3o_1) → (4, 4e_0)	336.3732	23	–	–
(5, 3o_1) → (5, 4e_0)	336.3804	24	–	–
(6, 3o_1) → (6, 4e_0)	336.3948	25	0.107 ± 0.207	0.049 ± 0.013
(7, 3o_1) → (7, 4e_0)	336.4197	26	–	0.341 ± 0.013
(8, 3o_1) → (8, 4e_0)	336.4520	27	1.806 ± 0.078	0.367 ± 0.014
(7, 1 − e_0) → (8, 1 − e_0)	336.9568	28	2.042 ± 0.072	0.414 ± 0.013
(7, 1 − o_1) → (8, 1 − o_1)	337.7278	29	–	–
(6, 5e_1) → (7, 6e_1)	353.9833	30	–	–

Notes. [a] e_0, o_1 and e_1 corresponds to the three first torsional states. The notation of the quantum numbers is directly taken from Mukhopadhyay (2016). [b] This corresponds to the number indicated in the top-right corner of each panel in Figures D.1 and D.2. [c] W is the integrated intensity of the unblended lines, summed over the range $[\nu_0 - \Delta\nu_{\rm FWHM}, \nu_0 + \Delta\nu_{\rm FWHM}]$, given $\Delta\nu_{\rm FWHM} = \nu_0 \frac{FWHM}{\rm c}$, with FWHM equal to 2.2 and 0.8 km s^{-1} for IRAS 16293A and B, respectively.

Appendix E: Synthetic spectra

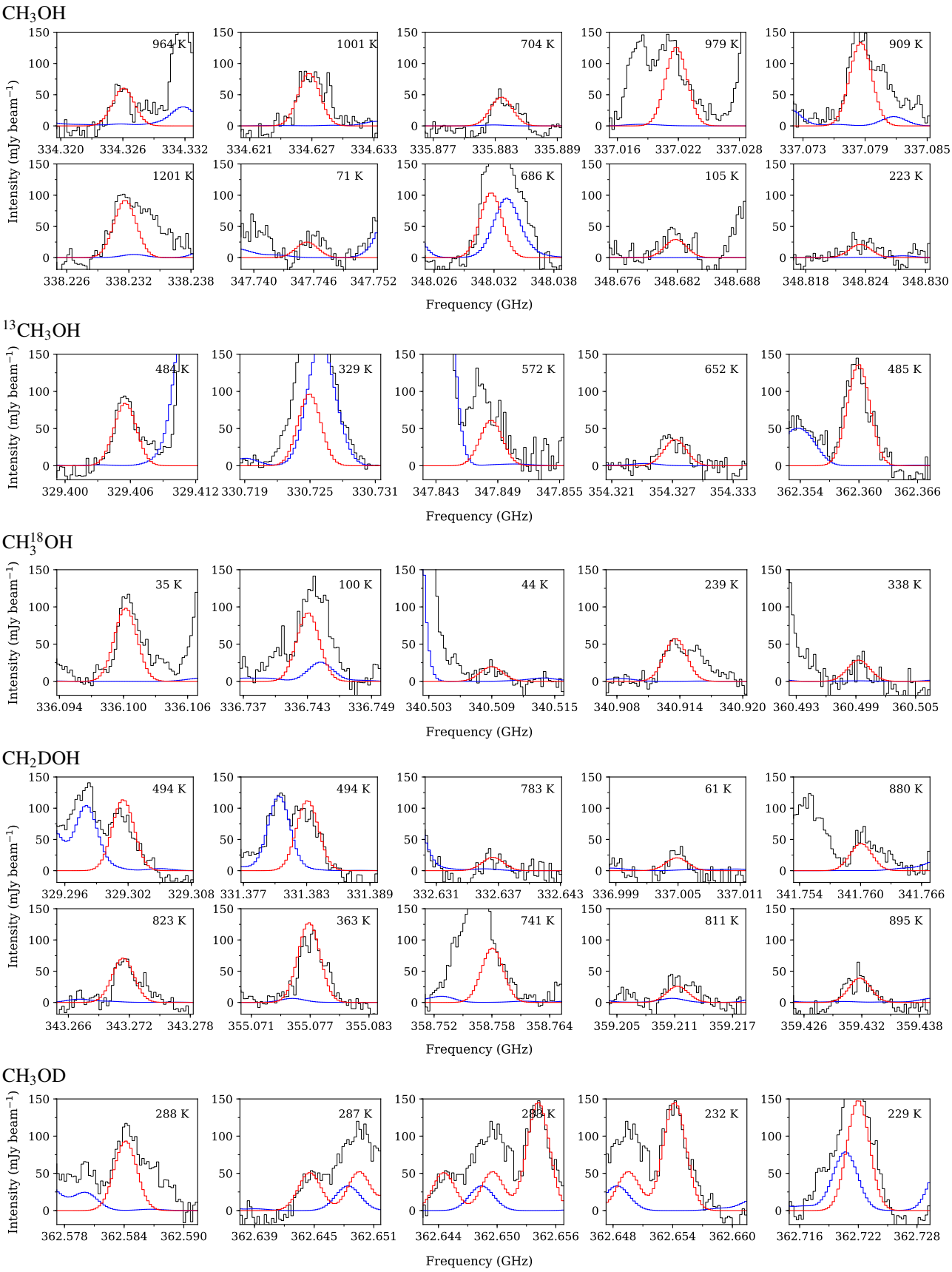


Fig. E.1: Representative selection of transitions of CH_3OH isotopologues towards IRAS 16293 A. The synthetic spectra is overplotted in red, the reference spectrum in blue, and the data in black. The upper energy level of the transition is indicated in the top-left corner.

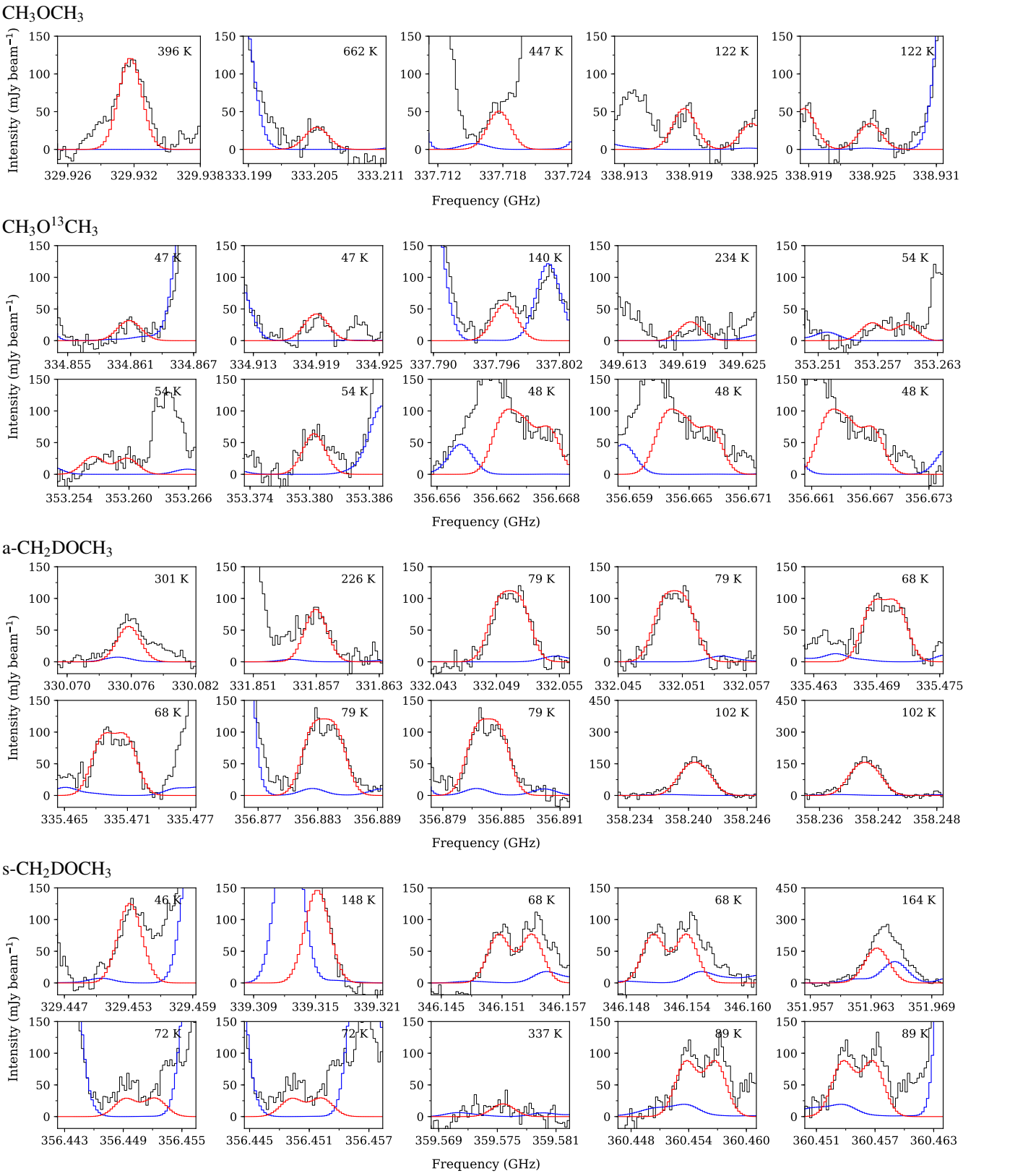


Fig. E.2: Representatives selection of transitions of CH_3OCH_3 isotopologues towards IRAS 16293 A. The synthetic spectra is overplotted in red, the reference spectrum in blue, and the data in black. The upper energy level of the transition is indicated in the top-left corner.

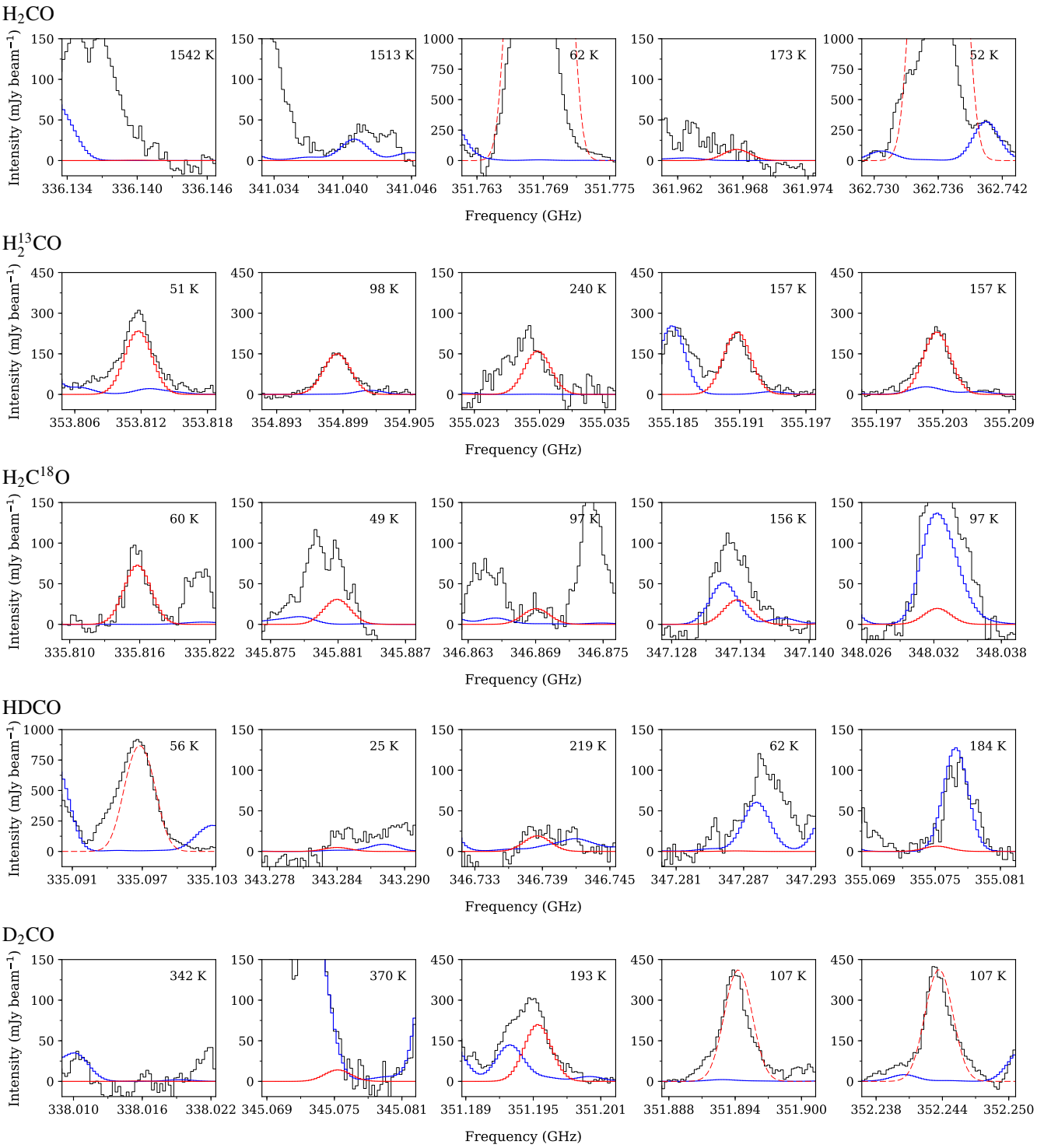


Fig. E.3: Representative selection of transitions of H_2CO isotopologues towards IRAS 16293A. The synthetic spectra is over-plotted in red, the reference spectrum in blue, and the data in black. The dashed curves represent optically thick lines. The upper energy level of the transition is indicated in the top-left corner.

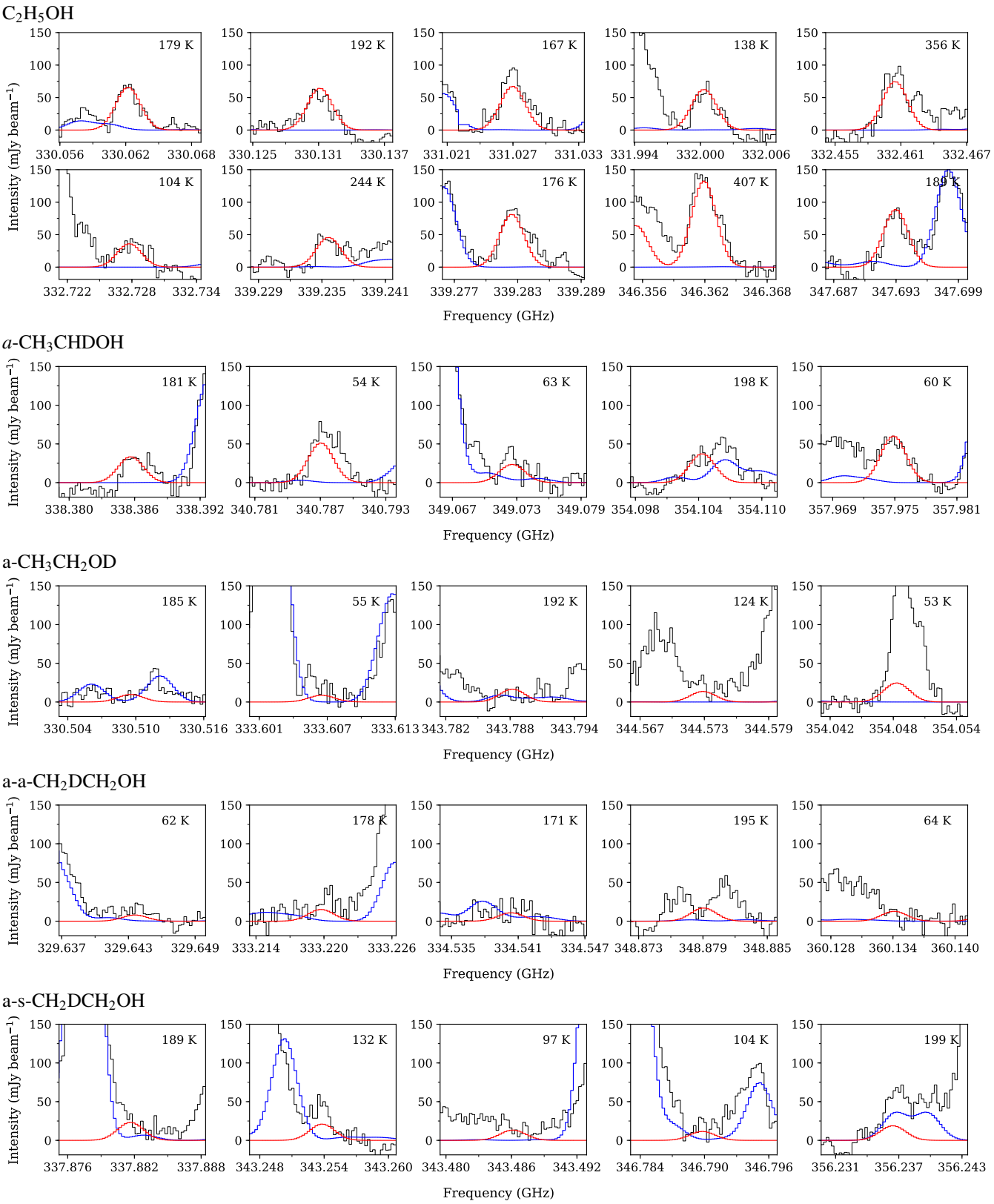


Fig. E.4: Representative selection of transitions of C_2H_5OH isotopologues towards IRAS 16293 A. The synthetic spectra is overplotted in red, the reference spectrum in blue, and the data in black. The upper energy level of the transition is indicated in the top-left corner.

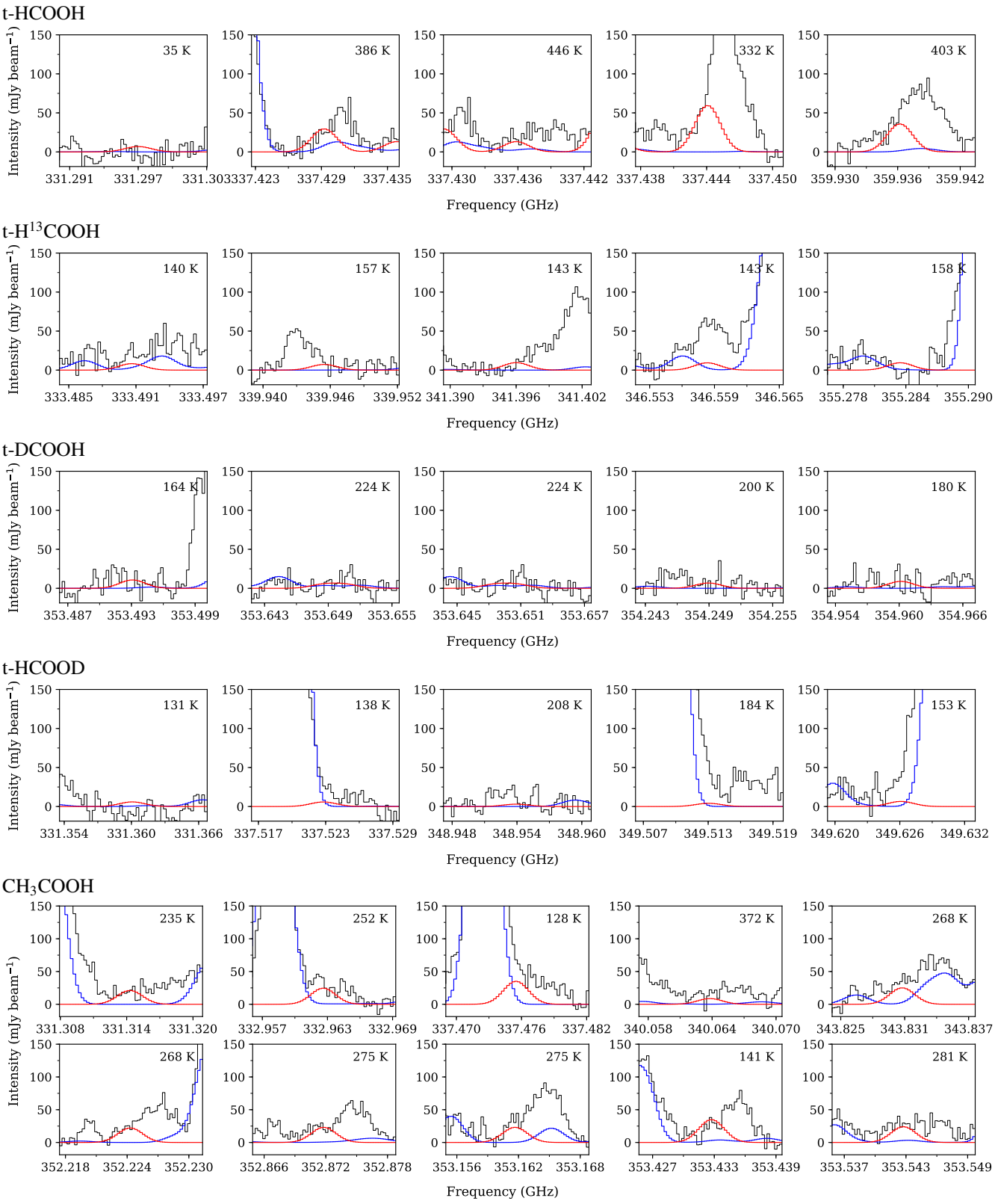


Fig. E.5: Representative selection of transitions of t-HCOOH isotopologues and CH_3COOH towards IRAS 16293 A. The synthetic spectra is over-plotted in red, the reference spectrum in blue, and the data in black. The upper energy level of the transition is indicated in the top-left corner.

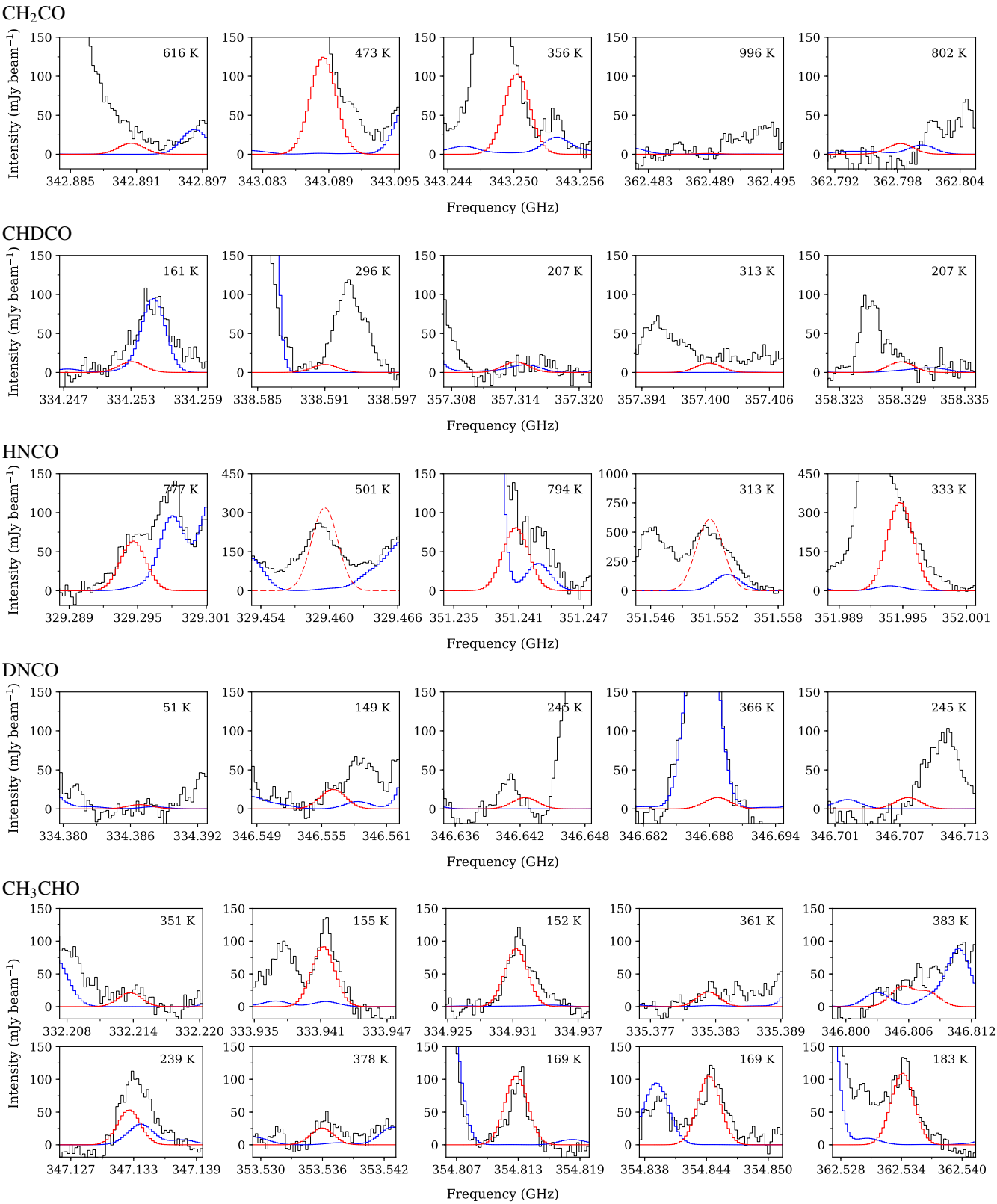


Fig. E.6: Representative selection of transitions of CH_2CO and HNCO isotopologues and CH_3CHO towards IRAS 16293 A. The synthetic spectra is over-plotted in red, the reference spectrum in blue, and the data in black. The upper energy level of the transition is indicated in the top-left corner.

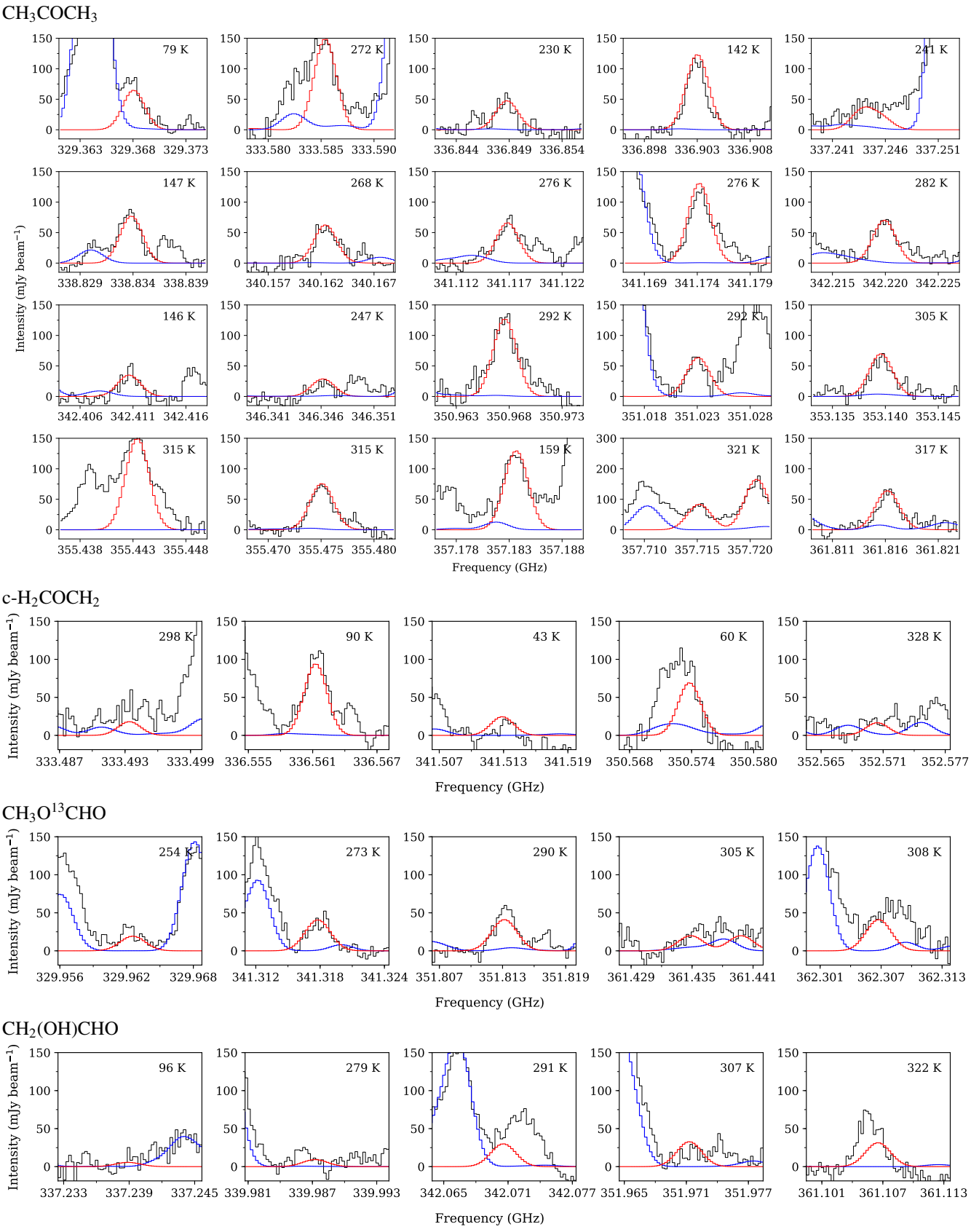


Fig. E.7: Representative selection of transitions of CH_3COCH_3, c-H_2COCH_2, $CH_3O^{13}CHO$, and $CH_2(OH)CHO$ towards IRAS 16293 A. The synthetic spectra is over-plotted in red, the reference spectrum in blue, and the data in black. The upper energy level of the transition is indicated in the top-left corner.

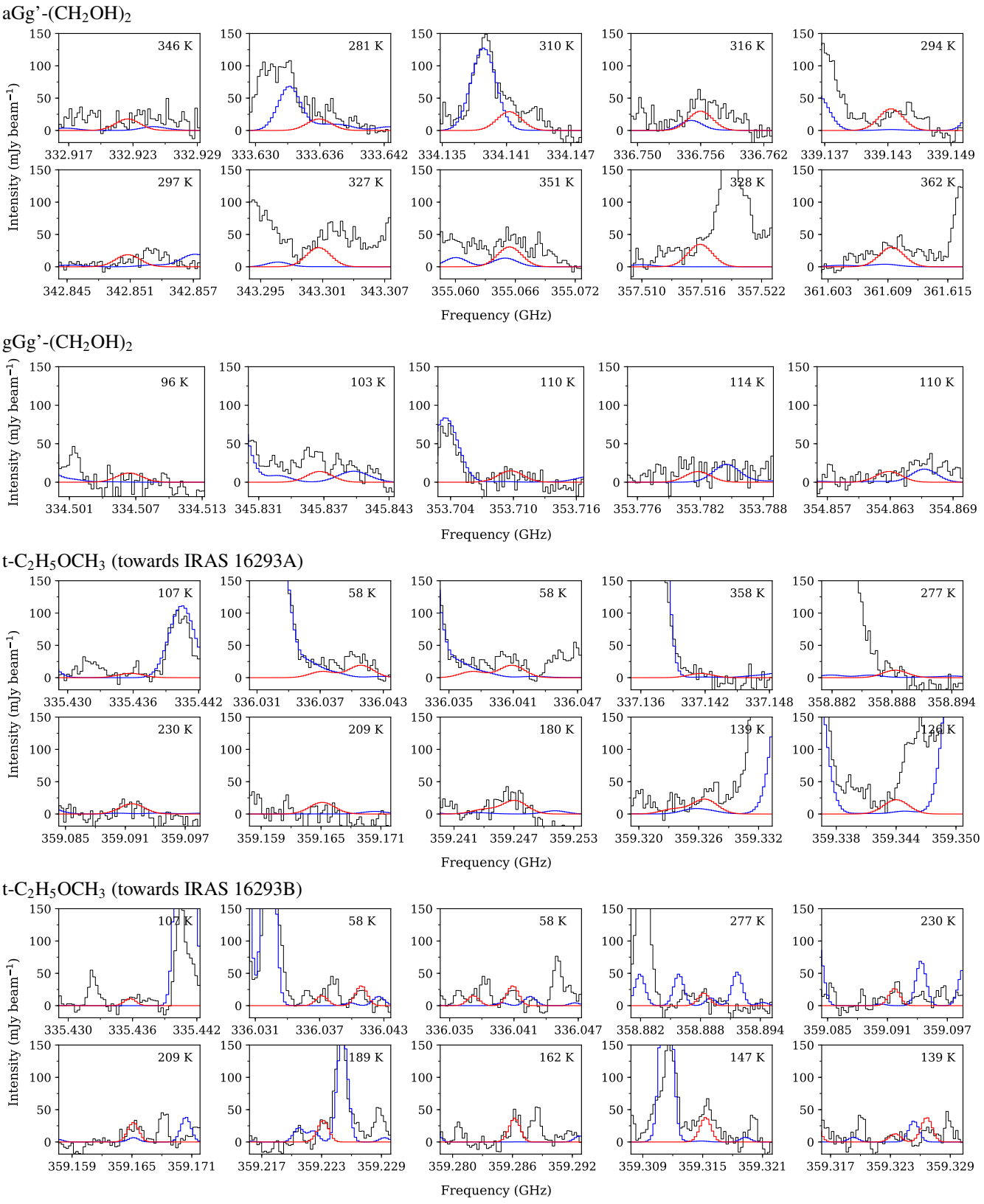


Fig. E.8: Representative selection of transitions of the two energetically lowest conformers of $(CH_2OH)_2$ towards IRAS 16293A and t-$C_2H_5OCH_3$ towards IRAS 16293 A and B. The synthetic spectra is over-plotted in red, the reference spectrum in blue, and the data in black. The upper energy level of the transition is indicated in the top-left corner.

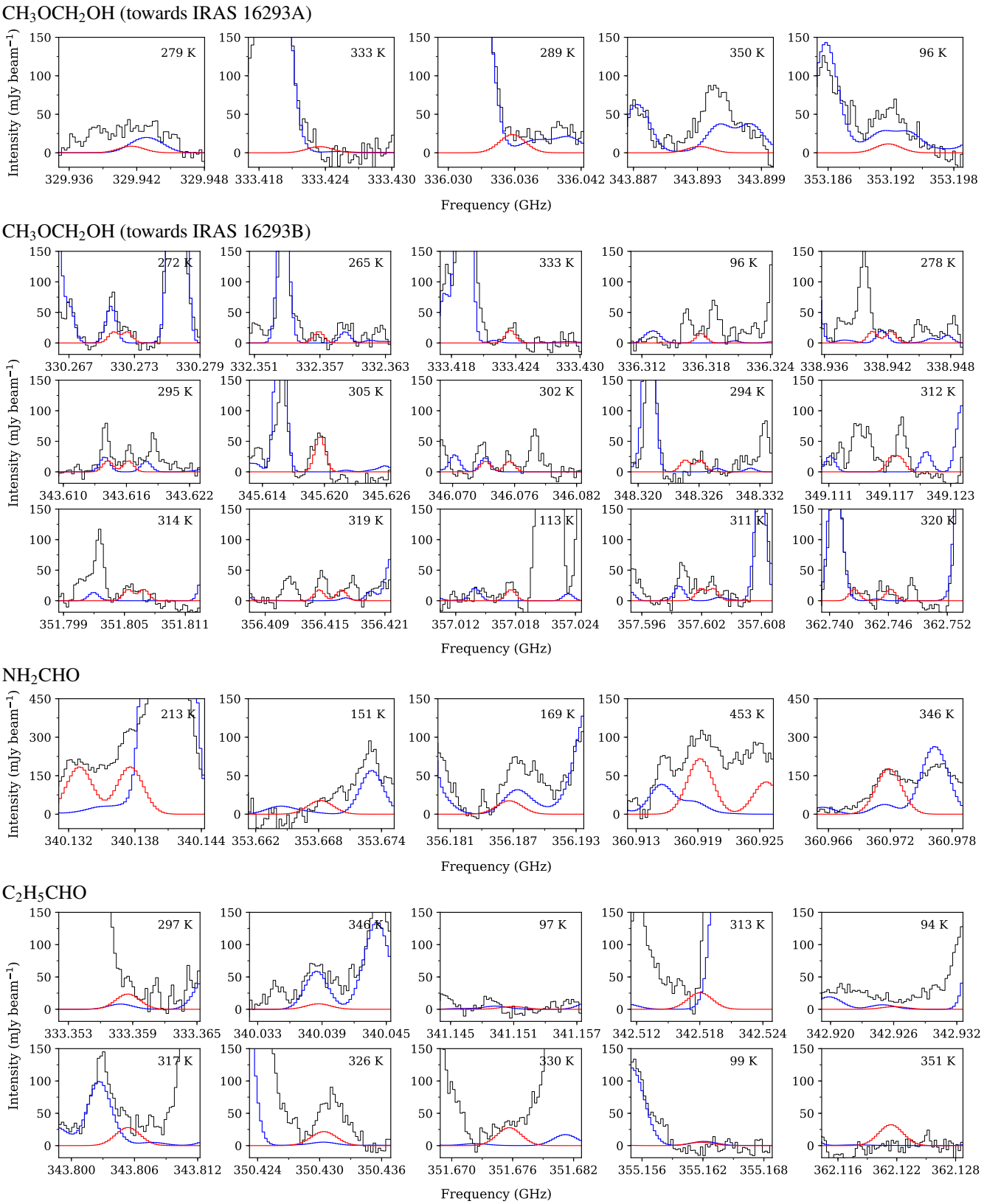


Fig. E.9: Representative selection of transitions of CH_3OCH_2OH towards IRAS 16293 A and B and NH_2CHO and C_2H_5CHO towards IRAS 16293A only. The synthetic spectra is over-plotted in red, the reference spectrum in blue, and the data in black. The upper energy level of the transition is indicated in the top-left corner.

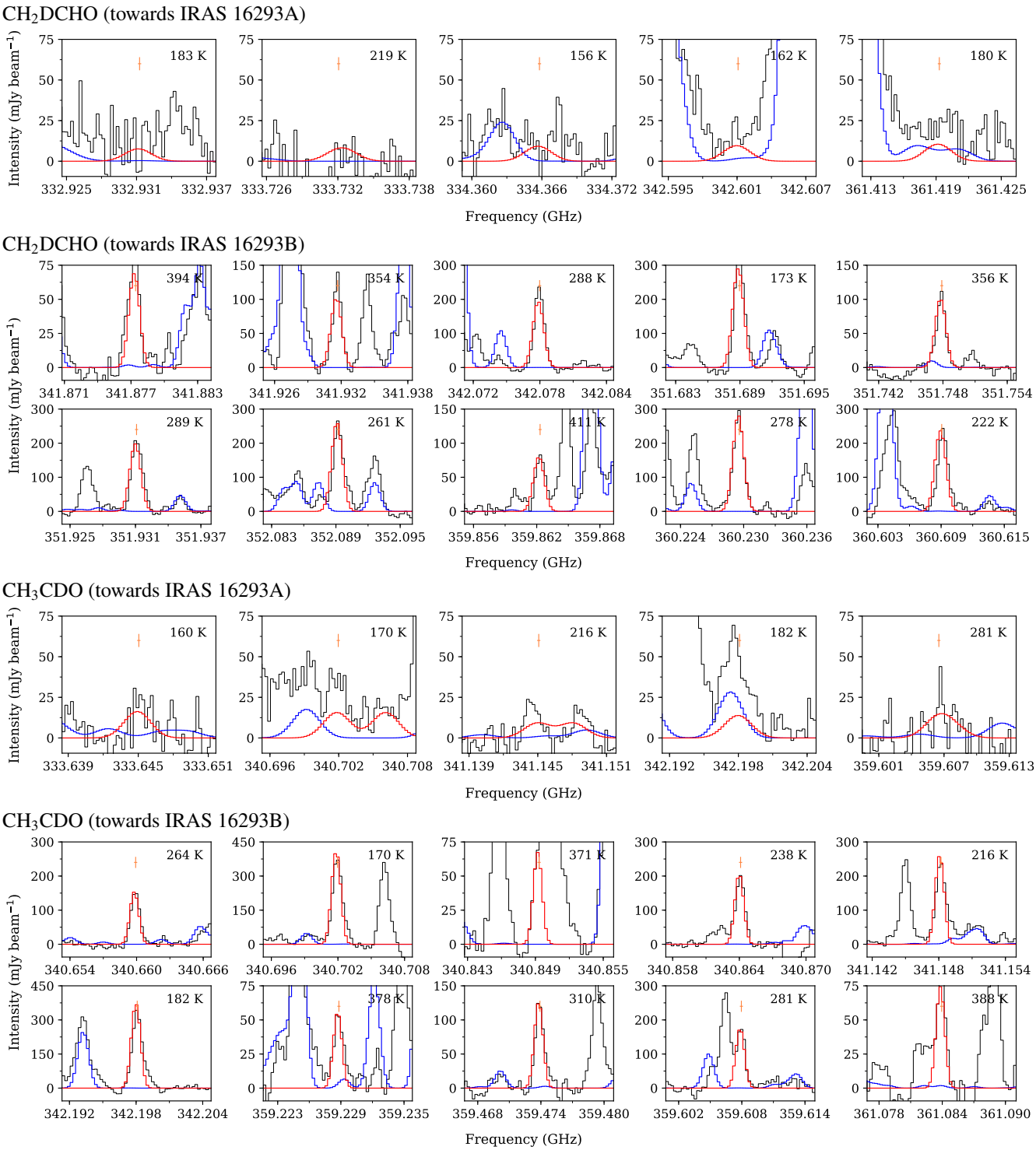


Fig. E.10: Representative selection of transitions of CH_2DCHO and CH_3CDO towards IRAS 16293 A and B. The synthetic spectra is over-plotted in red, the reference spectrum in blue, and the data in black. The upper energy level of the transition is indicated in the top-left corner.